

Towards imaging flow at the base of the mantle with seismic, mineral physics and geodynamic constraints

Andy Nowacki¹ and Sanne Cottaar²

¹School of Earth and Environment, University of Leeds, UK

²Department of Earth Sciences, University of Cambridge, UK

Abstract

Perhaps the least ambiguous signal that the mantle is convecting comes from observations of seismic anisotropy—the variation of wave speed with direction—which must arise due to the ordering of material as deformation occurs. Therefore significant effort has been made over many years to infer the direction and nature of mantle flow from these data. Observations have focussed on the boundary layers of the mantle, where deformation is expected to be strongest and where anisotropy is usually present. While prospects for mapping flow seem good, the lack of knowledge of several key issues currently holds progress back. These include the cause of anisotropy in the lowermost mantle, the causative material’s response to shear, and the single-crystal or -phase seismic properties of the causative materials. In this chapter we review recent observations of lowermost mantle anisotropy, constraints on mineral elasticity and deformation mechanisms, and challenges in linking geodynamic modelling with seismic observations.

1 Introduction

Seismic anisotropy, i.e. the variation of seismic velocity with propagation direction and polarisation, is observed in a number of regions within the Earth. The strength of anisotropy is particularly strong in the crust, at the top and the bottom of the mantle, and in the inner core (Mainprice, 2007). In the upper mantle, observed seismic anisotropy has been used to map asthenospheric flows (Becker and Lebedev, this volume) and understand slab dynamics (Huang and Zhao, this volume). In the lowermost mantle, understanding anisotropy in terms of flow is more elusive, as seismic observations are sparse, and mineral physical constraints more uncertain. The dynamics of the lowermost mantle are of particular interest, as they reflect the lower thermal and mechanical boundary layer of the convecting mantle. Mapping flow directions in this region would significantly help our understanding of the role of this boundary in mantle dynamics, and more specifically the role of the large low-shear velocity provinces (‘LLSVPs’) (Rudolph et al., this volume).

Albeit challenging, significant efforts have been made to use seismic anisotropy to understand the underlying crystal preferred orientations (CPO) and flow directions (e.g., Karato, 1998). This is based on the assumption that flow, and the internal crystallographic deformation mechanisms that accommodate the flow, cause alignment of intrinsically anisotropic crystals. This chapter offers a condensed review of seismic observations and mineral physical and geodynamical constraints on seismic anisotropy, and for a more in-depth review we refer to Nowacki et al. (2011) and Romanowicz & Wenk (2017). Here, we focus on the endeavours, mainly over the last decade, to tie these disciplines together and map flow directions in the lowermost mantle, and the specific challenges posed when comparing these results to seismic observations.

2 Observational constraints on lowermost mantle flow

2.1 Global tomographic models

A number of tomographic modellers invert for seismic anisotropy in the lowermost mantle. Inverting the full anisotropic elastic tensor (i.e., all 21 parameters) is unfeasible. The only component of anisotropy generally inverted for in the lowermost mantle is the velocity difference between horizontally polarised shear velocity, V_{SH} , and vertically polarised shear velocity, V_{SV} . This component of anisotropy is named radial anisotropy (or vertically transverse isotropy) and the degree of anisotropy can be expressed by the value $\xi = V_{SH}^2/V_{SV}^2 = C_{66}/C_{44}$, where C is the Voigt matrix representation of elasticity and the 3-axis is vertical.

For the upper mantle, radial anisotropy is well constrained due to the unique sensitivities of the two types of surface waves (Becker and Lebedev, *this volume*). For the lower mantle, one or both of normal modes and body waves must be used. Normal mode inversions for 1D radial models show no significant component of ξ (Beghein et al., 2006; de Wit & Trampert, 2015). 3D tomographic models show a mainly isotropic lower mantle with lateral variations in ξ on the order of 0.97–1.03 in the lowermost mantle (e.g., Moulik & Ekstrom, 2014; Auer et al., 2014; Chang et al., 2015; French & Romanowicz, 2015). There are strong differences between these models, some of which can be attributed to their treatment of the crust in the inversion, which is shown to affect the radial anisotropic signature of the lowermost mantle (Ferreira et al., 2010; Panning et al., 2010). In general, a geographical trend emerges where $\xi > 1$ (equivalently, $V_{SH} > V_{SV}$) in regions with fast shear wave velocity interpreted to be slab graveyards, and opposite signature of $\xi < 1$ is seen in regions of slow shear wave velocity, i.e. the LLSVPs. In Figure 1 this relationship is illustrated with histograms of ξ values for the fast and slow regions as interpreted by Cottaar & Lekić (2016), as well as a vote map of ξ values, which at each point at 2800 km depth shows the count of all tomography models which have a value of ξ above or below 1. While all models show a significant shift in their histograms for the fast and slow region, the shifts between their mean values is small, with the largest shift of 1.1% in SEMUCBwm1, and the smallest shift of 0.38% in SAVANI. The vote map also suggests a relationship between dV_S and ξ . Interpreting this general trend should be done with caution as any relationship between dV_S and ξ could be an artefact of the inversion, specifically the negative ξ values appear prone to be leakage of the slow isotropic velocities (Chang et al., 2015). One thing that is interesting to note from the vote map is the smaller slow shear region beneath the Ural mountains, dubbed the Perm anomaly (Lekić et al., 2012), does not correlate directly with a signal of $\xi < 1$, but a small anomaly showing $\xi < 1$ appears offset to the south.

Studies are even more limited in constraining P wave radial anisotropy ($\phi = V_{PV}^2/V_{PH}^2 = C_{33}/C_{11}$). Global studies constraining 1D radial P wave anisotropy show no agreement in the likely signature (Beghein et al., 2006; de Wit & Trampert, 2015). Global 3D studies have often applied an assumed scaling between the S and P wave anisotropy as a starting model. When they do include P wave radial anisotropy independently (Soldati et al., 2003; Tesoniero et al., 2016), they judge their results not to be robust. Inversions using body waves are heavily under-constrained (Boschi & Dziewoński, 2000). The synthetic study of P. J. Koelemeijer et al. (2012) shows general sensitivity of normal modes to P wave anisotropy, although it also predicts it is sensitive to trade-offs.

A potential way forward for global studies lies in the understanding of a third anisotropic parameter, $\eta = C_{13}/(C_{11} - 2C_{44})$, which is related to the S and P velocities at intermediate incidence angles. de Wit & Trampert (2015) show that this parameter has a robust 1D signature of $\eta < 1$ across the lower 1000 km of the mantle. Kawakatsu (2015) suggests a rewrite of η for a more physical relationship with wave incidence angle, and shows that constraining this parameter, η_κ , can help resolve whether horizontally isotropic layers could cause the observed anisotropy.

2.2 Regional body wave observations

Locally, deep mantle seismic anisotropy can be observed through shear wave splitting of body waves. One of the main challenges is to determine the relative contribution to splitting from the uppermost and lowermost mantle, and whilst often assuming the rest of the lower mantle is isotropic. A general approach is to use two seismic phases with comparable ray paths across the upper mantle, while one reference phase has a different or no ray path across the lowermost mantle. Ideally the reference phase shows no or minimal splitting and all splitting in the other phase

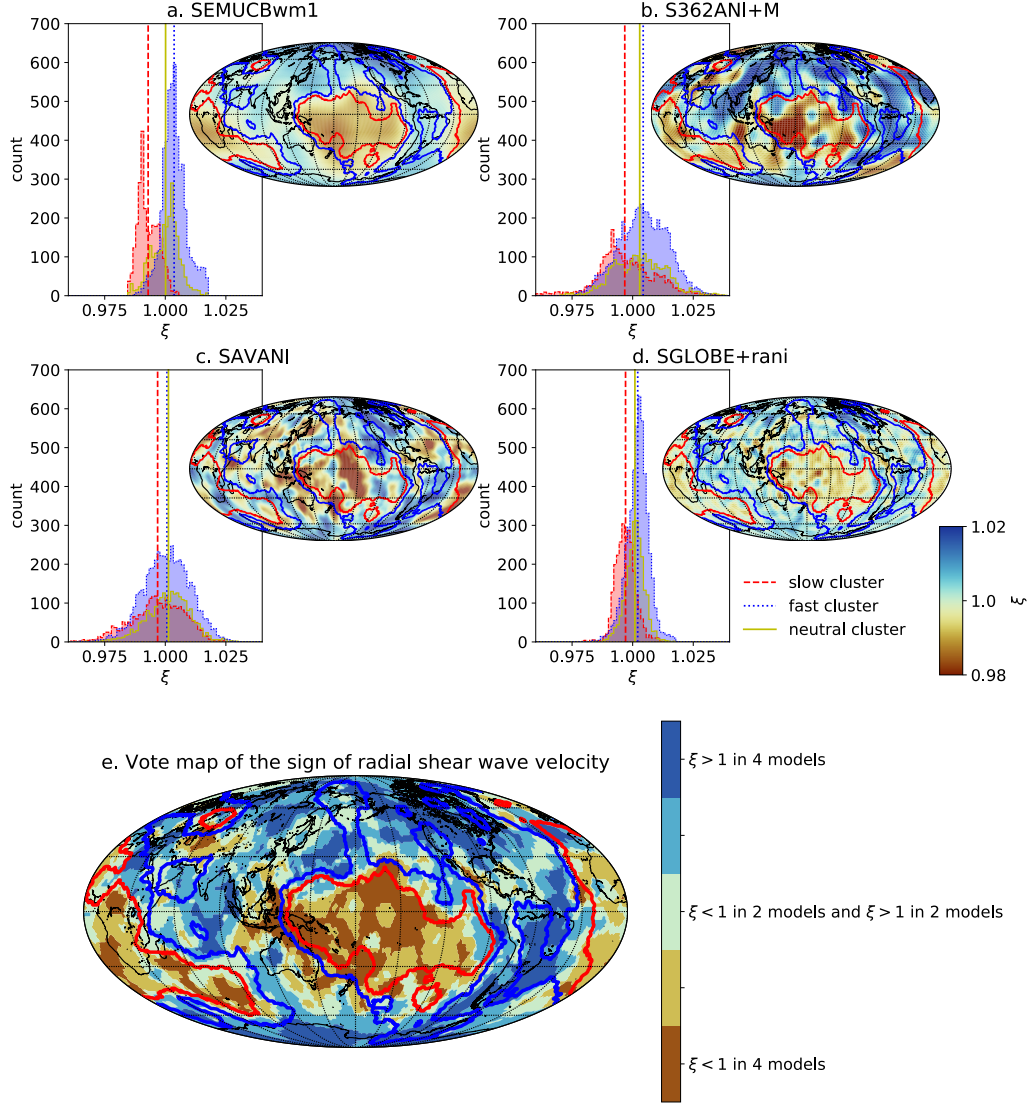


Figure 1. a. -d. Maps show shear wave radial anisotropic parameter ξ at 2800 km depth for SEMUCBwm1 (French and Romanowicz, 2014), S362ANI+M (Moulik and Ekstrom 2014), SAVANI (Auer et al. 2014), SGLOBE-rani (Chang et al., 2015). Red and blue contours show bounds at three votes for the isotropic slow and fast cluster based on votes across five isotropic models (Cottaar & Lekić, 2016). Histograms show distribution and mean values of ξ in the different cluster vote areas, red-‘slow’, blue-‘fast’, yellow-‘neutral’ (boundaries for ‘neutral’ cluster are not shown on the maps). e. Vote map showing where models agree on $\xi > 1$ or $\xi < 1$ (V_{SH} or V_{SV} being faster, respectively). All models agree that $\xi > 1$ for 18% of the map, while for $\xi < 1$ the area is 13%.

can be attributed to the lowermost mantle. Otherwise corrections for splitting from the upper mantle need to be applied to attribute splitting to the lower mantle (e.g., Wookey et al., 2005).

One potential set consists of the ScS and S phases (Figure 2). For the distance range of 60–85°, the S phase turns above the lowermost mantle, while the ScS phase samples the lowermost mantle (e.g., Lay & Young, 1991; Wookey & Kendall, 2008). A second set is the SKS and SKKS phases (at epicentral distances 108–122°), for which the ray paths exit the core at different locations and converge across the mantle (e.g., Niu & Perez, 2004; Wang & Wen, 2007; M. Long, 2009). SKS–SKKS pairs have the additional advantages over S–ScS that in an isotropic or radially-anisotropic mantle they exit the core purely polarised along the SV component, and any anisotropy along the down-going leg of the path can be ignored. Their disadvantage is that both phases can accrue splitting in the lowermost mantle and in the upper mantle. At times it is difficult to retrieve splitting parameters and these phases are usually only used to highlight discrepant phase pairs (e.g., Deng et al., 2017).

Lastly, S_{diff} phases (at 100–130° distance) are compared either to S/ScS at shorter distances, or to SKKS (or SKS) at longer distances (e.g., Kendall & Silver, 1996; Vinnik et al., 1998). The SV component of the diffracted wave attenuates much faster than the SH along the core-mantle boundary, which means S_{diff} at large distances ($> \sim 120^\circ$) becomes a purely SH polarised wave, and any splitting can be attributed to the upgoing leg of the ray path (Cottaar & Romanowicz, 2013).

In all cases, caution is required in interpreting body-wave observations if modelled using approximate methods such as ray theory, since shear waves at the base of the mantle have a large region of finite-frequency sensitivity. For S_{diff} , travel time differences between SH_{diff} and SV_{diff} can arise for purely isotropic models, especially with strong isotropic velocity gradients as one might expect due to the thermal boundary layer, due to different finite-frequency sensitivity of the two components along the boundary (Maupin, 1994; Komatitsch et al., 2010; Borgeaud et al., 2016; Parisi et al., 2018). ScS suffers to a lesser extent from finite-frequency effects in 1D models, but ray theoretical interpretations can badly misrepresent the strength and orientation of anisotropy when lateral variations in anisotropy may exist (Nowacki & Wookey, 2016).

The different phases have different sensitivity to the anisotropic tensor due to their propagation angle and the length of their propagating path across the lowermost mantle (Figure 2). S_{diff} has long horizontal propagation paths in the mantle, and therefore good sensitivity to radial anisotropy. SKS propagates at sub-vertical angles (18°–33°) across the lowermost mantle, so splitting is caused by the component of azimuthal anisotropy, i.e. variation of wave speed in the horizontal plane. SKKS (40°–50°) and ScS (62°–78°) propagate at intermediate angles, and are sensitive to tilted anisotropy. While early studies focused mainly on constraining the radial anisotropic component (e.g., Young & Lay, 1990; Matzel et al., 1996; Garnero & Lay, 1997), recent studies interpret their observations as tilted anisotropy, the main component constrained when accounting for the incidence angles in the lowermost mantle (e.g., Thomas et al., 2007; Wookey & Kendall, 2008; Nowacki et al., 2010).

One additional, unique type of observation worth mentioning are polarity observations of phases bouncing off of the so-called D'' discontinuities in the lowermost mantle (Thomas et al., 2011; Cobden & Thomas, 2013; Creasy et al., 2019; Pisconti et al., 2019). Azimuthal variations in the polarity measurements suggest these are sensitive to underlying anisotropy. As observations can be applied to S and P reflections (‘SdS’, and ‘PdP’), they are to our knowledge the only body wave studies that have resolved a component of both S and P wave anisotropy for a single location.

Most observational studies focus on a single observational method, as well as a single azimuthal direction. To sufficiently constrain anisotropy in a single location to uniquely interpret flow direction, multiple techniques need to be combined (Creasy et al., 2019). Efforts have been made to target a single region from multiple angles using ScS (Nowacki et al., 2010; Wookey & Kendall, 2008) and polarisation measurements

(Thomas et al., 2011), as well as combining multiple angles with multiple body wave phases (Ford & Long, 2015; Creasy et al., 2019; Wolf et al., 2019).

2.3 Observed regional anisotropy

This is not an exhaustive overview of body wave studies and for a full table of studies we refer to Romanowicz & Wenk (2017). Here we highlight consistencies across these studies, mainly focusing on more recent studies which benefit from increased coverage by seismic arrays. Regional body wave studies largely agree with tomographic models on geographical trends in radial anisotropy, i.e. $\xi > 1$ where isotropic velocities are fast, and $\xi < 1$ where isotropic velocities are slow (e.g., Wookey & Kendall, 2007; Kawai & Geller, 2010). Models interpreting tilted anisotropy have overwhelmingly sampled isotropically fast areas and many find a sub-horizontal fast axis and thus a component of $\xi > 1$ (e.g., Thomas et al., 2007; Garnero et al., 2004; Wookey & Dobson, 2008; Nowacki et al., 2010), while several studies find a fast axis which is tilted from the horizontal by around 45° (Wookey et al., 2005; Cottaar & Romanowicz, 2013), which is not compatible with radial anisotropy. Particularly, regions just outside of LLSVPs appear to have strong and variable anisotropy, as is observed along the boundaries of the African LLSVP (Wang & Wen, 2007; Cottaar & Romanowicz, 2013; Lynner & Long, 2014; Grund & Ritter, 2019; Romanowicz & Wenk, 2017; Reiss et al., 2019), the Pacific LLSVP (Deng et al., 2017), and the Perm Anomaly (M. D. Long & Lynner, 2015). These observations show stronger anisotropy outside of the LLSVP and little to no anisotropy within the LLSVP, both in terms of tilted anisotropy (Cottaar & Romanowicz, 2013) and in terms of azimuthal anisotropy (e.g., Lynner & Long, 2014; Grund & Ritter, 2019). A change in sign from $\xi > 1$ to $\xi < 1$ is also observed towards the base of the Icelandic plume (Wolf et al., 2019).

While some consistency emerges on the types of anisotropy, and correlations with isotropic velocities, uncertainty lies in the strength of anisotropy observed. Tomographic models contain radial anisotropy on the order of several %, and amplitudes vary between models (see Figure 1). Local observations interpret tilted anisotropy of 0.8–1.5% across a layer of 250 km beneath North America (Nowacki et al., 2010) and up to 8% across 150 km beneath the Antarctic Ocean (Cottaar & Romanowicz, 2013). Such variations could represent true geographical observations, but biases could also occur as propagation angles used might not be optimal to observe the strongest splitting or assumed layer thicknesses. In these two example studies, interpreted amplitudes might also differ as one is interpreted ray-theoretically (Nowacki et al., 2010) and one by forward modelling (Cottaar & Romanowicz, 2013). Potentially, consistently constrained relative amplitudes in splitting might help map lateral variations in flow strength or direction.

3 Forward modelling

To provide synthetic tests for the hypothesis that anisotropy is caused by crystal preferred orientation (CPO), multi-disciplinary models are built that span many spatial scales (see flow chart in Figure 3). Geodynamic models provide maps of strain across 10s to 1000s of km. The strain observed is accommodated on the micro scale by deformation mechanisms in a set of crystals, assuming a degree is accommodated by dislocation glide to create preferential orientation. The individual elastic constants of each of the deformed set of crystals are averaged using their orientations, giving the fully anisotropic tensor for a single location. This process needs to be repeated for many locations, to provide an anisotropic model with signatures that can be observed over 10s or 100s of km by seismic waves. Here we explain the main choices and assumptions made in these models.

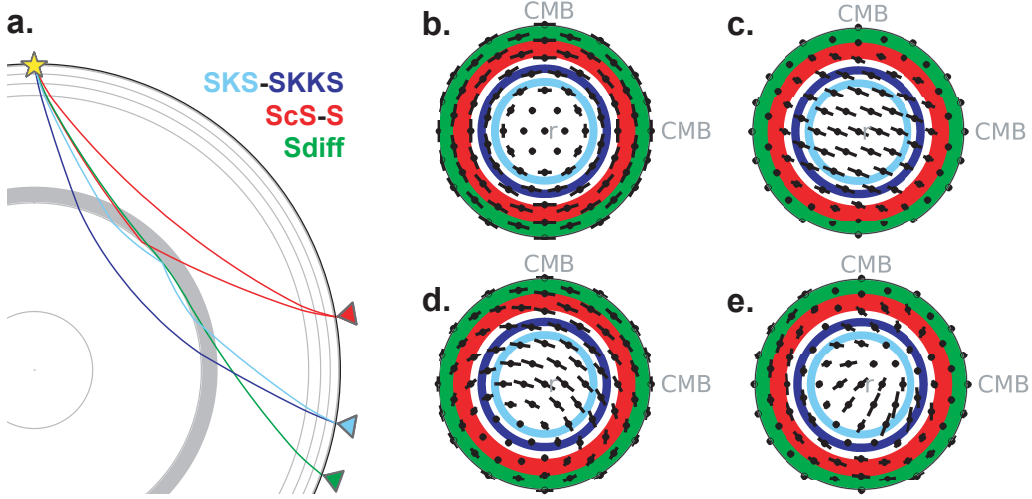


Figure 2. a. Ray paths for general body wave (pairs) used to constrain lowermost mantle anisotropy: SKS-SKKS (blue), ScS-S (red), S_{diff} (green) (made with Obspy; Krischer et al., 2015). b.-e. Hemisphere projections of various assumed anisotropic symmetries viewed from above (made with MSAT; Walker & Wookey, 2012). Bars show splitting direction and bar lengths show splitting strength as a function of shear wave propagation direction. Coloured shading shows general sensitivity of body waves (see a.) although there is some overlap. b. Radial anisotropy with $\xi = 1.03$ c. 3% azimuthal anisotropy with a fast axis direction of 112° . d. Tilted anisotropy, i.e. anisotropy in c. tilted by 40° . e. Full anisotropic tensor for 75% post-perovskite and 25% periclase in a downgoing slab (see Section 4.2).

While we focus on the hypothesis that CPO is the cause of seismic anisotropy in the lowermost mantle, studies have forward modelled the potential of shape preferred orientation (SPO) as well. SPO anisotropy is caused by layering or inclusions of strongly heterogeneous (but potentially intrinsically isotropic) material (Kendall & Silver, 1998; Hall et al., 2004; Creasy et al., 2019; Reiss et al., 2019). In the case of inclusions, anisotropy can be observed in the effective medium to which the waves are sensitive if a degree of alignment or preferred orientation persists over a broad area. This alignment of inclusions would result from local deformation, and thus also contain information about mantle flow. However, studies observing high frequency scatterers in the lowermost mantle observe very weak velocity contrasts ($<0.1\%$; Mancinelli & Shearer, 2013). Extremely strong isotropic velocity anomalies (10–30%) are only observed in thin patches of several 10s of km on top of the core–mantle boundary, the so-called ultra-low velocity zones (e.g., Garnero et al., 1998; Yu & Garnero, 2018).

3.1 Geodynamic models

Assumptions on the flow occurring in the lowermost mantle have varying degrees of complexities. In the simplest of models, horizontal flow is assumed causing simple horizontal shear as one might expect in a iso-chemical thermal boundary layer (as used in Wookey & Kendall, 2007). Anisotropy observed, however, does not have to represent local deformation, but could represent fossilized anisotropy. Anisotropic material can be formed elsewhere and be transported and rotated without overriding the preferred orientation. Therefore it is important to track the history of deformation for material in a given location. To represent change in flow direction in downwellings

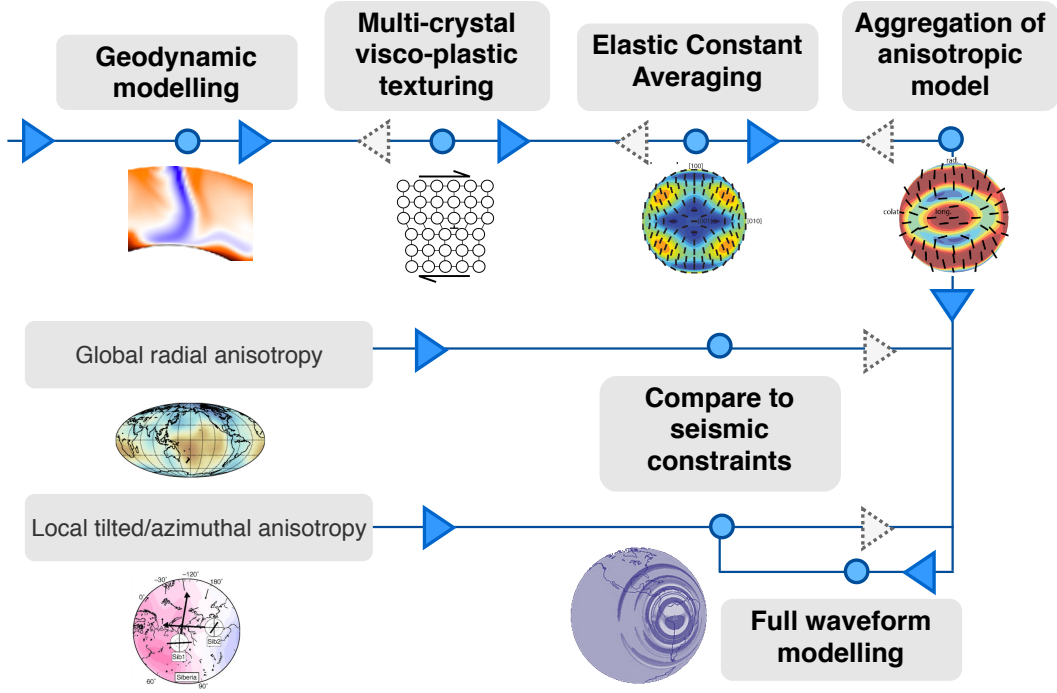


Figure 3. Showing the general steps in forward modelling from a flow model to interpreting seismic observations following the filled blue arrows as discussed in Section 3. Dashed arrows indicate the inverse steps to go from seismic observations to flow directions, for which challenges and limitations are discussed in Section 5

and upwellings in the lowermost mantle, corner flow streamlines can be used (Tommasi et al., 2018).

A range of studies use fully numerical models, where a number of assumptions on parameters for the lower mantle need to be made. The history of deformation is tracked by passive tracers that are advected through the model and record the velocity gradient at each step. The deformation history is generally used from the top of the lower mantle (e.g., Cottaar et al., 2014), or from the bridgmanite to post-perovskite transition (e.g Walker et al., 2011).

In one approach (Cottaar et al., 2014; Chandler et al., 2018), the CitcomS program (Zhong et al., 2000) is used to solve for the conservation of mass, momentum and energy, in a system that is heated from below, and where a slab is forced down from the top. Tracers are introduced at the top of the slab, and a large number of them eventually end up in the lowermost mantle, although the final distribution is irregular and shows clumping of tracers.

In a different approach (Walker et al., 2011; Nowacki et al., 2013), the flow field is the instantaneous flow predicted by isotropic wave velocities, the gravity field, a 1D viscosity model, and other geophysical constraints (Simmons et al., 2009). Because the inversion assumes that flow does not change with time, regularly-spaced tracers can be back-propagated to the top of D'' across the flow field, after which they are forward propagated to track the deformation along the path. The advantage of this method is that one retrieves a regularly-sampled global anisotropic model that holds some potential relationship to the isotropic velocities, and that can thus be compared to global or regional seismic observations. Additionally, this method tests a prior

assumed relationship between isotropic velocities and the flow field, testing models of thermal and/or thermo-chemical heterogeneity in the lower mantle.

While these geodynamical models represent test cases to explain lowermost seismic anisotropy, they are simplified in many ways. The geodynamical models have not explicitly included the bridgmanite to post-perovskite transitions, which only has a small density jump (Murakami et al., 2004; Oganov & Ono, 2004), but would cause significant viscosity weakening (Hunt et al., 2009) and allow slab material to spread more easily (Nakagawa & Tackley, 2011). The viscosity model would be even more complex if the formation of CPO could be fed back into the geodynamical model creating anisotropic viscosity. So far, models have not tested the hypothesis of LLSVPs representing a different composition (e.g., Garnero et al., 2016), which appears important to understand the laterally varying anisotropy around LLSVP boundaries.

3.2 Mineralogical constraints

In the upper mantle, the mineral olivine is abundant, and, with a highly anisotropic crystal, represents a straightforward candidate to explain CPO anisotropy (Becker and Lebedev, this volume). For the lowermost mantle the debate is still open as to which mineral or polymineralic assemblage can explain the observed anisotropy. For a candidate mineral or assemblage, we need to know its single crystal elasticity, which depending on crystal symmetry can be described by three to 21 independent parameters. We mostly rely on first-principle or *ab initio* calculations which solve the electronic Schrödinger equation to obtain the crystal structure and the elasticity at high pressures and temperatures (Buchen, this volume). Merely obtaining isotropic average elasticity information from experiments under these extreme conditions is very challenging, let alone measuring the independent anisotropic parameters (e.g., Marquardt et al., 2009; Finkelstein et al., 2018).

Additionally, we need to know how the candidate mineral or assemblage deforms (Miyagi, this volume). To create seismic anisotropy, a mineral must significantly deform by dislocation glide. In dislocation glide, dislocations within the crystal move along crystallographic planes. Preferred orientation results when crystals rotate to accommodate glide along its weakest glide planes. Other mechanisms like diffusion creep or dislocation climb are not usually thought to cause preferred orientation, though this is not always the case (Wheeler, 2009, 2010; Dobson et al., 2019). If dislocation glide is the preferred mechanism, the next question that arises is what are the relative strengths of the different slip systems (i.e., glide plane and slip directions). Calculations explore the relative strengths of different deformation mechanisms and glide systems by calculating lattice friction and forces required to slip a dislocation (Peierls stress) in atomistic models (Walker et al., 2010; Cordier et al., 2012). Experimentally, slip system activities cannot usually be measured for single crystals of the phases of interest here. Instead, materials are deformed under compressive or shear stress in a large-volume apparatus (usually on analogue materials), or in a diamond-anvil cell (For further details Miyagi, 2020; Romanowicz & Wenk, 2017). The resulting deformation may be imaged by X-ray diffraction. Dominant slip systems may be estimated by inspection of the orientation distribution functions (ODFs) of the crystallographic planes of interest, or inverted for by comparing forward calculations of the experimental deformation with the results obtained.

To determine macroscopic anisotropy from these mineralogical constraints, the set of slip systems are combined with a deformation tensor to model a set of deformed crystals. Most often this is done using a homogenisation method such as the viscoplastic self-consistent method (VPSC; Lebensohn & Tomé, 1993).

Forming the majority of the lowermost mantle, and thus the likeliest candidates to be the anisotropy-causing phases, are bridgmanite, post-perovskite and ferropericlase.

3.2.1 *Bridgmanite*

Bridgmanite, (Mg,Fe)SiO₃-perovskite, is the most abundant mineral in the lower mantle (and in the Earth). Its pure Mg-endmember shows $\sim 11\%$ P wave and up to 15% S wave anisotropy (Oganov et al., 2001; Wentzcovitch et al., 2006; Stackhouse, Brodholt, Wookey, et al., 2005), and shows little (Li et al., 2005; Zhang et al., 2016) or variable (Fu et al., 2019) variation with the inclusion of iron.

There are mixed results on bridgmanite being a suitable candidate to explain anisotropy. Both experiments and calculations proposed a dominant glide plane of (001) (Wenk et al., 2004; Merkel et al., 2007; Ferré et al., 2007) which results in the opposite radial anisotropy to that observed (e.g., Wenk et al., 2011), while other experiments and calculations argue for a dominant (100) glide plane (Mainprice et al., 2008; Tsujino et al., 2016), which can create the observed $V_{SH} > V_{SV}$ in simple shear. Miyagi & Wenk (2016) report a change from (001)-dominated glide to (100) around 55 GPa.

Bridgmanite is also known to be a very strong mineral. Experiments deforming a multi-phase mixture of bridgmanite and a smaller fraction of the weaker phase ferropericlase (or analogs), show in some cases that the ferropericlase takes up the majority of the deformation (Girard et al., 2016; Kaercher et al., 2016; Miyagi & Wenk, 2016), while in others the strong bridgmanite phase still dominates deformation (Wang et al., 2013) in line with simulations in a finite element model (Madi et al., 2005). Recently atomistic calculations have shown that the resistance to dislocation glide is very high, and dislocation climb should dominate (Boioli et al., 2017). Dislocation climb dominance could explain the general lack of anisotropy across most of the lower mantle, as well the high viscosity of the lower mantle (Reali et al., 2019). However, attempts to explain weak anisotropy around ponded subducted slabs in the uppermost lower mantle in terms of bridgmanite CPO (Tsujino et al., 2016; Walpole et al., 2017; Ferreira et al., 2019; Fu et al., 2019) would be therefore puzzling.

3.2.2 *Post-perovskite*

Post-perovskite is a high-pressure polymorph of bridgmanite, which could become stable in the lowermost mantle (Murakami et al., 2004; Oganov & Ono, 2004). Compared to bridgmanite, post-perovskite is (1) more anisotropic (Itaka et al., 2004; Stackhouse, Brodholt, & Price, 2005; Wentzcovitch et al., 2006; Zhang et al., 2016), and (2) much weaker to deform (Hunt et al., 2009; Ammann et al., 2010; Goryaeva et al., 2016). Therefore it is an attractive candidate to explain anisotropy observed in the lowermost mantle. If, and to what degree, post-perovskite is actually stable at the pressures in the lowermost mantle is still up for debate (see overviews in Cobden et al. (2015) and Hirose et al. (2015)), but invoking the presence of post-perovskite helps explain S-to-P velocity ratios in the lowermost mantle (P. Koelemeijer et al., 2018). If present, the strongly positive Clapeyron slope of its phase transition from bridgmanite implies post-perovskite is stable in a thicker layer in cold regions than in hot regions (Oganov & Ono, 2004; Tsuchiya et al., 2004). Potentially post-perovskite becomes unstable again in the thermal boundary layer close to the core-mantle boundary, creating a lens of post-perovskite (Hernlund et al., 2005).

Testing post-perovskite as a candidate to explain anisotropy is difficult as the preferred slip system of post-perovskite is uncertain and diamond-anvil cell experimental results have varied widely over the past 15 years (For further details, see

Miyagi, 2020, in this volume.). The most recent results can be split in two categories. Experiments using MgSiO_3 post-perovskite, and MnGeO_3 or MgGeO_3 analogs, show a preferred slip plane of (001) (e.g., Miyagi et al., 2010; Hirose et al., 2010; Nisr et al., 2012; X. Wu et al., 2017). Experiments using CaIrO_3 postperovskite as an analog show a dominant slip system of $[100](010)$ (where $[hkl]$ gives the Burgers vector; e.g., Yamazaki et al., 2006; Niwa et al., 2012; Hunt et al., 2016). Atomistic models confirm the results of the latter category, showing both slip systems $[100](010)$ and $[001](010)$ (Cordier et al., 2012; Goryaeva et al., 2015, 2017) as well as the occurrence of twinning $1/2 < 110 > \{1\bar{1}0\}$ (Carrez et al., 2017). Additionally, it is suggested that post-perovskite could inherit preferred orientation or texture through the phase transition from bridgmanite (Dobson et al., 2013). Interpretation of the texture inheritance in deformation experiments has been specifically argued to explain part of the variation in interpreted preferred glide plane (e.g., Walte et al., 2009; Miyagi et al., 2011). This could only be the case if bridgmanite forms CPO texture due to dislocation glide, which is debatable (Boioli et al., 2017). A more feasible scenario is bridgmanite inheriting texture from post-perovskite in a reverse transition which could occur in the hotter regions (Dobson et al., 2013; Walker et al., 2018).

The importance of the incorporation of aluminium and iron into post-perovskite for our purposes depends on its effect on the stability field, deformation mechanisms, rheology and single-crystal anisotropy of the non-endmember phase. Iron- and aluminium-bearing post-perovskite is likely to be as anisotropic as the magnesian end-member at lowermost mantle conditions (Mao et al., 2010; Caracas et al., 2010; Zhang et al., 2016), but there is little evidence for its effect on plasticity. Recent work suggests that iron will strongly partition into ferropericlase in the lowermost mantle in any event (Gialampouki et al., 2018), thus its importance may be limited.

3.2.3 *Ferropericlase*

Ferropericlase $(\text{Mg, Fe})\text{O}$ is present in the lower mantle with a molar abundance of 10–30% (e.g., McDonough & Sun, 1995). Before post-perovskite was discovered in 2004, ferropericlase was already considered a potential explanation of lowermost mantle anisotropy (Yamazaki & Karato, 2002). It is cubic, and its elasticity can thus be described by three independent parameters. These are constrained both through *ab initio* calculations (Karki et al., 2000; Z. Wu et al., 2013) and through experiments (e.g., Jackson et al., 2006). The results of these studies show significant single crystal anisotropy, as well as an increase of anisotropy with Fe content, related to changes in C_{12} and C_{44} with cell volume via pressure (Marquardt et al., 2009; Antonangeli et al., 2011; Finkelstein et al., 2018).

Ferropericlase is much weaker than bridgmanite (Cordier et al., 2012). Atomistic calculations of pure MgO endmember have shown dominating slip systems of $\langle 110 \rangle \{1\bar{1}0\}$ and $\langle 110 \rangle \{100\}$ (Carrez et al., 2009; Amodeo et al., 2011, 2016). Experiments on pure MgO (Merkel et al., 2002; Girard et al., 2012) and $(\text{Mg, Fe})\text{O}$ (Lin et al., 2009) show dominant slip on $\langle 110 \rangle \{1\bar{1}0\}$, while higher temperature experiments on $(\text{Mg, Fe})\text{O}$ also activate $\langle 110 \rangle \{100\}$, consistent with the calculations. Whether ferropericlase can explain the observed anisotropy depends on the degree of single crystal anisotropy (related to the Fe content), its abundance in the lowermost mantle (i.e. whether ferropericlase grains become interconnected), and the general strength contrast between ferropericlase and bridgmanite or post-perovskite. However, it should be noted that even in the two-phase experiments discussed earlier, where ferropericlase takes up the bulk of the deformation, coherent CPO does not develop in the ferropericlase, potentially due to the polyphase geometry causing strain heterogeneity in the ferropericlase crystals (Kaercher et al., 2016; Miyagi & Wenk, 2016).

3.2.4 Other phases

Whilst post-perovskite, bridgmanite and ferropericlase are expected to dominate the lowermost mantle, it is possible that other phases play a role in causing anisotropy.

Though peridotite comprises $\sim 5\%$ of Ca-perovskite (CaMgSiO_3) in the lower mantle, basaltic compositions may hold up to 30% (McDonough & Sun, 1995), and hence Ca-pv may be important if subducted material can accumulate at the base of the mantle. Sample recovery issues mean that high-pressure and -temperature experiments are difficult and the phase boundary between cubic and tetragonal Ca-pv is still being determined (Thomson et al., 2019), but molecular dynamics simulations (Li et al., 2006) show maximum single-crystal shear wave anisotropy of 25%, similar to other phases mentioned here. Room-temperature diamond-anvil cell experiments (Miyagi et al., 2009) and Peierls–Nabarro modelling (Ferré et al., 2009) suggest Ca-pv might form a CPO in deformation by glide on the cubic slip system $\langle 1\bar{1}0 \rangle \{110\}$, and experiments on the analogue CaGeO_3 suggest Ca-perovskite may be weaker than MgO (Wang et al., 2013), but relatively few studies have yet examined this further.

Silica phases may also make up $\sim 20\%$ of a basaltic lower mantle. While it seems likely that stishovite is stable until about 1500 km depth, uncertainty remains as to when in the lower mantle silica transitions from the CaCl_2 structure to seifertite (e.g., Sun et al., 2019). This may be important since whilst seifertite appears to be only moderately anisotropic (Karki et al., 1997) and hence is likely not be a large contributor to lowermost mantle anisotropy, CaCl_2 -type silica may have much stronger shear wave anisotropy of about 30% (Yang & Wu, 2014). Unfortunately we do not currently have constraints on how silica phases may accommodate strain.

If hydrogen can be carried to the deep mantle, then hydrous phases such as aluminous phase D or phase H might occur in D'' (e.g., Pamato et al., 2015; Panero & Caracas, 2017), whilst aluminous phase $\delta\text{-AlOOH}$ is likely present in basaltic compositions (e.g., Duan et al., 2018), and iron-rich regions could contain Fe-rich phases such as FeO_2 or FeOOH (e.g., Hu et al., 2016). Some of these phases may be strongly anisotropic, however compared to the nominally anhydrous silicates like bridgmanite and post-perovskite, little work has been done to understand their deformation mechanisms.

4 Joint geodynamic–seismic modelling

4.1 Recent developments

Several endeavours—mainly over the last decade—have tried to tie together all the fields and constraints discussed so far, in order to interpret anisotropy in the lowermost mantle. The long-term, sometimes enigmatic, goal of these studies is to map flow directions in the lowermost mantle to understand its role in the overall mantle convection (as the title of this chapter suggests). Most studies to this date, however, attempt to constrain the underlying cause of anisotropy taking their best guess at the flow regime.

In terms of the cause of anisotropy, recent studies rely heavily on post-perovskite being stable in the lowermost mantle to explain the observed anisotropy, arguing that bridgmanite produces the wrong radial anisotropic signature, and ferropericlase is not abundant enough to dominate anisotropic signatures. Bridgmanite not playing a major role can also be argued in light of the recent results that bridgmanite is too strong to cause dislocation glide and develop preferred orientation (Boioli et al., 2017).

The dominant glide plane in post-perovskite that is argued to explain anisotropy varies with studies arguing for dominant glide on (010) (Walker et al., 2011; Nowacki

et al., 2013; Creasy et al., 2017; Tommasi et al., 2018; Ford et al., 2015) and (001) (Nowacki et al., 2010; Cottaar et al., 2014; Walker et al., 2018; X. Wu et al., 2017; Chandler et al., 2018). These studies range from finding a best fitting model from a qualitative comparison to previously published observations (i.e., Cottaar et al., 2014; Tommasi et al., 2018) to a quantitative misfit with local observations (Nowacki et al., 2010; Ford et al., 2015; Creasy et al., 2017) or with global anisotropic models (Walker et al., 2011, 2018). Of course, all of these studies have made different assumptions and choices, which may affect the final conclusion. One example is the choice of elastic constants—for instance, a dominant glide system on the (010) plane results in $V_{SH} > V_{SV}$ when using elastic constants of Stackhouse, Brodholt, & Price (2005), and in $V_{SV} > V_{SH}$ when using those of Wentzcovitch et al. (2006) (Yamazaki & Karato, 2007; Wenk et al., 2011). Similarly, studies may choose to use constants derived at a single pressure and temperature—not necessarily those of the part of the mantle of interest—or attempt to include the variable anisotropic effects as P and T vary (Walker et al., 2011).

A number of recent studies are worth highlighting. Tommasi et al. (2018) explore the anisotropy resulting from deformation constraints from atomistic modelling instead of experimental results, arguing for a dominant glide plane of (010). Atomistic calculations, which will hopefully converge with experimental results in the future, offer a great step forward into constraining the deformation in the lowermost mantle. Their modelling finds weak radial anisotropy of $V_{SH} > V_{SV}$ and sub-horizontal fast polarization directions in simple corner flow.

Their modelled elastic tensors with post-perovskite and periclase in an upwelling tracer can also fit the recent observations of changing anisotropy beneath Iceland by Wolf et al. (2019). However, the paper also presents models of pure bridgmanite and periclase that can fit the observations for the assumed change in flow.

Walker et al. (2018) explore texture inheritance from (001) slip in post-perovskite to bridgmanite (Dobson et al., 2013) on a global scale. Such a model can explain the observed sharp changes in the signature of anisotropy from regions dominated by cold downwellings, to regions dominated by hot upwellings or LLSVPs. Comparable results for texture inheritance were shown by Chandler et al. (2018) using the tracking of single tracers from downwelling to upwelling.

Most of the studies mentioned have pre-assumed the flow pattern either locally or globally and the models of different compositions are tested against seismic observations. Only the studies of Ford et al. (2015) and Creasy et al. (2017) both fit the compositional model as well as the flow direction. For both cases, this is applied to one locality where anisotropy is constrained from different azimuthal directions. Ford et al. (2015) suggest mainly vertical flows occur just to the East of the African LLSVP, while Creasy et al. (2017) suggest horizontal flows in a region of fast isotropic velocities beneath New Zealand and Australia.

4.2 Example case: comparing a model to seismic observations

Many of the multi-disciplinary modelling studies discussed above compare their synthetic elasticity models to ray-theoretically derived local body wave observations. A number of studies explore the limitations of interpreting body waves observations in terms of anisotropy by analysing synthetic observations; for example for 1D isotropic or radially anisotropic models for S_{diff} waves (Maupin, 1994; Komatitsch et al., 2010; Borgeaud et al., 2016; Parisi et al., 2018) and for ScS waves (Kawai & Geller, 2010). Nowacki & Wookey (2016) extend the analysis for ScS waves to full synthetic anisotropic models with small-scale variations from the model of Walker et al. (2011) (cf. Figure 3). They conclude that ray-theoretical interpretations hold up for the simplest anisotropic models, but break down for those with variable anisotropy. Additionally,

the finite-frequency wave senses less splitting than a ray-theoretical interpretation of an anisotropic model would suggest, as the finite-frequency sensitivity will average over the strongly varying anisotropic medium, sensing an effective medium.

Here we explore these limitations further by combining the forward modelling in a subducting slab of Cottaar et al. (2014) with the full-wave modelling of Nowacki & Wookey (2016) and analyse S_{diff} , ScS, SKS, and SKKS phases in a finite-frequency framework.

4.2.1 Geodynamic and texture modelling

We use the results of Cottaar et al. (2014). We refer the reader to the original work for a full description of parameters used, but note that in this type of modelling, uncertainty can be introduced via a number of parameters including: the chosen relative critical resolved shear stresses on each slip system; the lack of a non-glide mechanism to accommodate strain and reset texture (such as diffusion creep); the phase boundary between phases; the single-crystal elastic constants; and the stress-strain homogenisation scheme. In the following we give a short summary of the modelling details.

Deformation is tracked along tracer particles (Figure 4a) across the lowermost mantle using CitcomS (Zhong et al., 2000), where 500 grains are modelled with the viscoplastic self-consistent method (VPSC; Lebensohn & Tomé, 1993) to accommodate the deformation. 75% of these grains are post-perovskite ('ppv') or bridgmanite ('pv'), and 25% are periclase. For post-perovskite, a dominant glide plane of (100) ('ppv 100' model), (010) ('ppv 010'), or (001) ('ppv 001') is assumed. The assumed glide planes for periclase are weaker, and this phase ends up accommodating 35-40% of the deformation. For the elastic constants, the values of Stackhouse, Brodholt, Wookey, et al. (2005) are used for post-perovskite and bridgmanite, and those of Karki et al. (2000) for periclase. Cottaar et al. (2014) note that model ppv 001 is in general agreement with the radial anisotropy observed at the bottom of slabs and fast directions of azimuthal anisotropy is parallel to flow directions. The radial anisotropy in model ppv 010 also has the right sign, but is very weak in nature.

4.2.2 Seismic modelling

We seek to compare the predicted seismic characteristics of our geodynamic slab model to regional observations of anisotropy, including splitting in S_{diff} , SKS-SKKS and S-ScS differential splitting, as well as observations of changes in splitting intensity (Chevrot, 2000). In order to do this, we simulate the propagation of waves through the model in two directions—along the slab and across it—for a range of geometries. We use synthetics in the epicentral distance range $55^\circ \leq \Delta \leq 80^\circ$ for ScS, $100^\circ \leq \Delta \leq 130^\circ$ for SKS, $110^\circ \leq \Delta \leq 130^\circ$ for SKKS and $95^\circ \leq \Delta \leq 120^\circ$ for S_{diff} . Table 1 outlines the geometries used in this study and which phases are investigated for each, whilst Figure 4b shows the location of the events and receivers.

We calculate the seismic response of the slab using the spectral element method as implemented in the SPECFEM3D_GLOBE code (Komatitsch & Tromp, 2002). In order to remove time in writing intermediate files, we use a version of the code where creating the spectral element mesh and solving the equations of motion are performed in the same program (Komatitsch et al., 2003; Nowacki & Wookey, 2016). We use two chunks of the cubed sphere with 800 spectral elements along each side, giving seismograms accurate at frequencies below 0.2 Hz, similar to the dominant period of the waves at these distances.

The elasticity model is mapped to the seismic computational mesh by finding the nearest neighbouring tracer particle within a defined 'slab' region, which is below

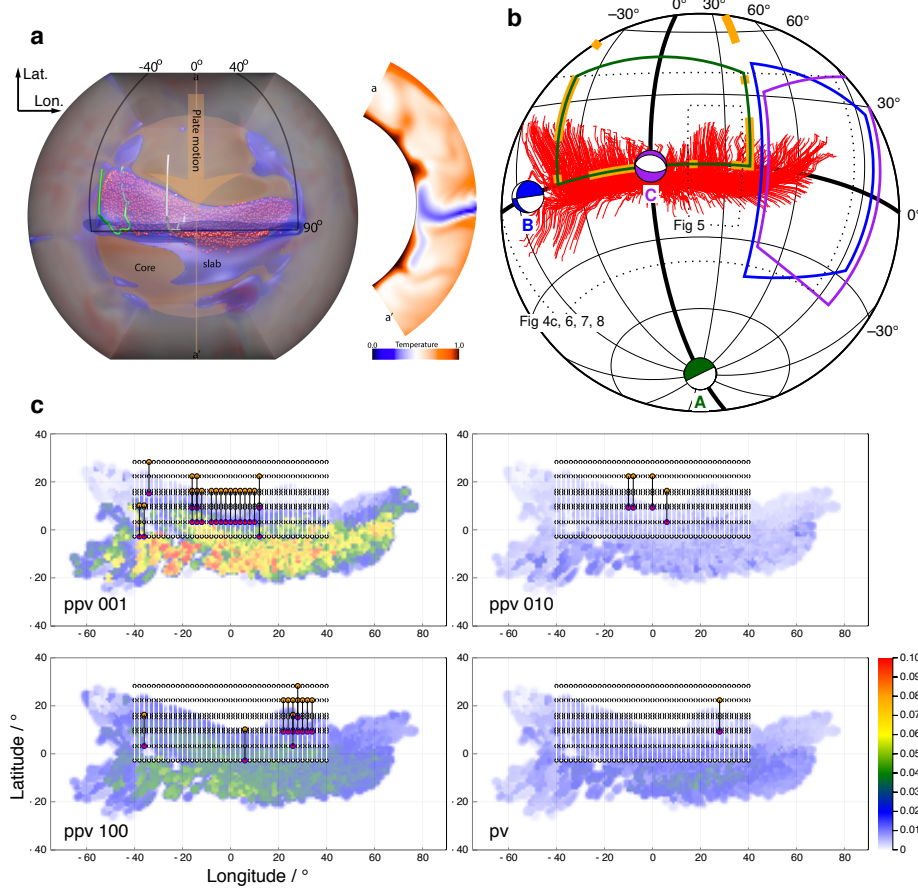


Figure 4. (a) Geodynamical setup of forward calculation, taken from Figure 1 of Cottar et al. (2014). A slab is imposed, moving from north to south, which subducts along the equator. Tracer particles are shown by orange dots, with the path for two highlighted as green and white lines. Section a–a′ along longitude 0° to the right shows non-dimensional temperature. (b) Geometry of synthetic seismic sources and receivers in relation to the slab model. Sources are shown by colour-coded lower-hemisphere focal mechanisms (annotated with the code in Table 1), matching the receiver locations, shown by open areas with solid boundaries. Red lines show the paths of tracer particles, and orange dash-dotted lines show the slab edges in panel (a). Areas shown by other figures are indicated by dotted black lines and labelled. (c) Discrepant SKS-SKKS splitting for path ‘A’ (Table 1) for each plasticity model. Red and orange circles respectively show the core piercing points for SKKS and SKS waves for pairs which are discrepant, whilst white circles denote the piercing points of pairs which are not. Underlying colour shows the strength of anisotropy at the bottom of the slab texture model, using the universal elastic anisotropy index, A^U (Ranganathan & Ostoja-Starzewski, 2008) according to the colour scale on the bottom right. (For approximate path lengths of SKS and SKKS in the lowermost mantle, see Figure 6.)

Table 1. Summary of synthetic paths used to investigate anisotropy in the geodynamic slab model.

Code	Description, phases ^a	Source longitude (°)	Source latitude (°)	Focal mechanism ^b
A	Across slab: SKS–SKKS	0	−90	090/0/−90
B	Along slab: SKS–SKKS, S _{diff}	−55	0	180/30/0
C	Along slab: ScS, S _{diff}	0	0	280/30/−90

^a Phases analysed from full-wavefield synthetics.^b Given as strike/dip/rake of the fault plane in °.

All events at 650 km depth.

400 km above the CMB and within 150 km from any given particle. Beyond this distance, the nearest particle’s elasticity grades smoothly to the background 1D velocity, given by AK135 (Kennett et al., 1995), over a 100 km distance using Voigt averaging between the isotropic and full elastic tensor. This smoothing distance was chosen to avoid artificially extending the region of the mantle influenced by the slab, whilst avoiding seismic artifacts from a spatially abrupt transition between isotropic and anisotropic mantle.

4.2.3 Synthetic analysis

We can process synthetics from our forward model in the same way as data and compare the two. For the purposes of this example, we show a selection of results for the three paths, for different combinations of seismic phases, analysing the shear wave splitting in ScS, S_{diff}, and differential splitting between SKS and SKKS. In all cases, we analyse the shear wave splitting in a window around the arrival of interest using the minimum-eigenvalue method of Silver & Chan (1991), with errors as updated by Walsh et al. (2013). The fast axis here is defined as the angle ϕ' from the radial component (or the vertical at the bottoming point of the seismic ray, Figure 1c in Nowacki et al. (2010)). We also consider the splitting intensity (SI; Chevrot, 2000) for SKS and SKKS waves, where the polarisation is known to be radial, and S_{diff} waves, where almost all SV energy is lost along the diffracted path, rendering them horizontally polarised. For this reason, S_{diff} SI is calculated in the opposite sense to usual for SK(K)S waves, interchanging the radial and transverse components in the calculation. Discrepant SKS–SKKS splitting pairs are identified where either one of the phases shows null splitting, whilst the other does within error, or the two phases’ 95% confidence region of the small-eigenvalue surface do not overlap. Additionally, for all splitting measurements we use the automatic classification method of Wuestefeld et al. (2010) to calculate Q , a measure of quality between −1 and 1. −1 indicates a null, 1 a good measurement, and 0 a likely poor measurement.

We consider first the splitting in ScS for path ‘C’ (Figure 5). This path is similar to observations of splitting along palaeosubduction zones such as beneath the Caribbean (Garnero et al., 2004; Maupin et al., 2005; Nowacki et al., 2010, e.g.). In general, it seems that $\phi' \approx 90^\circ$ ($\xi > 1$) in many slab regions (Nowacki et al., 2011; Romanowicz & Wenk, 2017); in the Caribbean in particular, Garnero et al. (2004) infer a systematic rotation in the fast angle across the palaeoslab region, giving a change in ϕ' from $\sim 105^\circ$ to $\sim 75^\circ$.

Returning to Figure 5, it is clear that plasticity models ppv 010 and ppv 100 are better candidates than the remaining models at reproducing the $V_{SH} > V_{SV}$ and variable ϕ' signals seen in data. Note that this is a different conclusion from Cottaar et

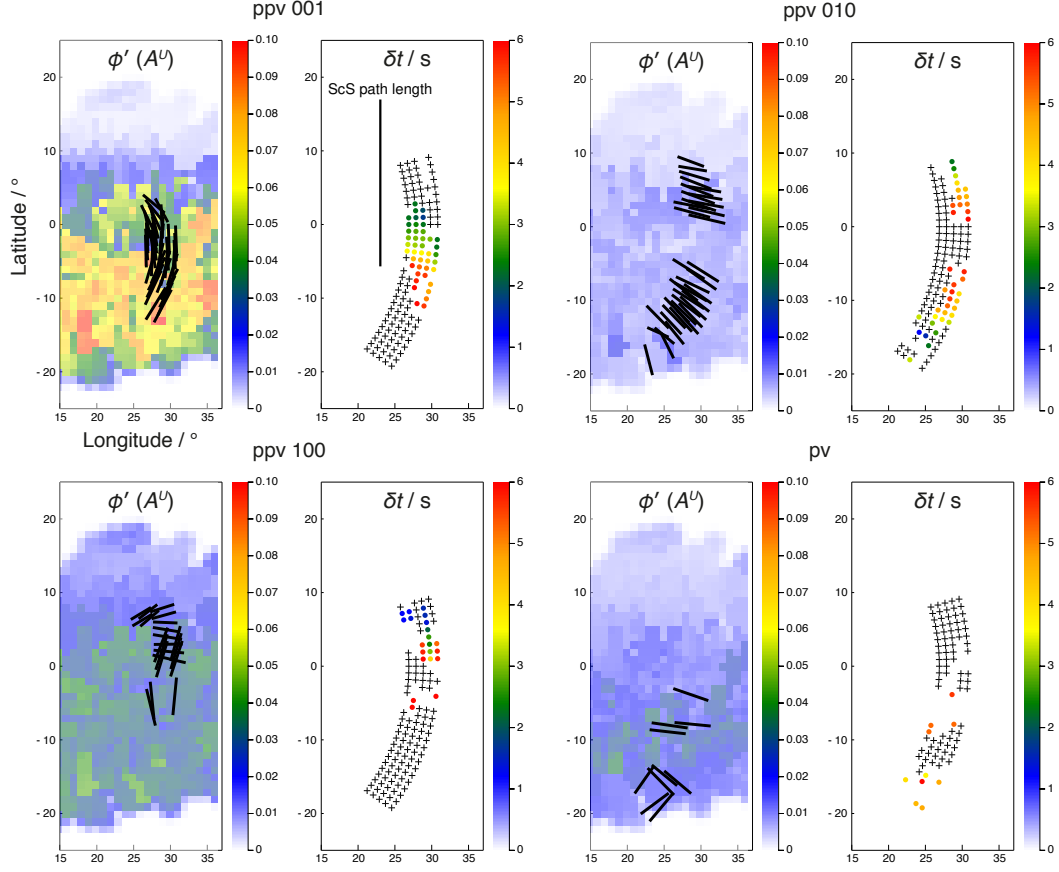


Figure 5. Shear-wave splitting results for the ScS phase for path ‘C’ (Table 1), for each slab texture. Each panel shows on the left the fast shear wave orientation in the ray frame (see Nowacki et al., 2010, Figure 1c), ϕ' , as a black bar located at the ScS core bounce point. Bars oriented left–right ($\phi' = 90^\circ$) correspond to radial anisotropy with $\xi > 1$, and vertical bars mean $\xi < 1$ ($\phi' = 0^\circ$), with non-radial anisotropy otherwise (when $0^\circ \neq \phi' \neq 90^\circ$). Colour beneath the bars is as in Figure 4c. On the right we show the amount of splitting, δt at each bounce point, coloured by the second scale bar. Crosses signify null measurements. The length of the ray path of ScS in the lowermost 250 km of the mantle is shown in the right hand panel for the ppv 001 case.

al. (2014), which could be due to the added complexity in this study of investigating the non-horizontal orientation of the waves, which can cause rotations in ϕ' (see Figure 2). The models produce values of δt which are mostly comparable to those seen in nature, though larger at up to 6 s in the synthetics versus $\sim 2\text{--}3$ s as observed. The strength of anisotropy present in the models is up to $A^U = 0.1$, which is about one-third of the predicted single crystal anisotropy of ppv in the lowermost mantle (Stackhouse, Brodholt, Wookey, et al., 2005).

We next show results for path ‘B’, which samples the slab similarly, but using S_{diff} and SKS–SKKS phases, in Figures 6 and 7. SI for S_{diff} should be large only when a significant non-radial anisotropy is present, which is generally the case within and at the edges of the slab.

It is notable in all cases that the pattern of ϕ' and δt is complex and variable across the slab, with large regions of null splitting even where strong anisotropy is present. Null splitting may occur when the polarisation of a shear wave travelling through an anisotropic medium is close to the fast or slow shear wave orientations (which are perpendicular) in that direction, and this may be the cause here. Variability in ϕ' is expected because of the pattern of flow in the model, and we observe fairly smooth rotations of ϕ' from north to south in the ppv models, similarly to data. However, the pv case shows δt variations do not correlate strongly to simple features in the elasticity model. This illustrates the sometime non-intuitive manner in which the seismic wave averages structure, and cautions against the use of approximate methods like ray theory when calculating synthetics in such models for data comparison.

SKS–SKKS pairs, in contrast, show relatively straightforward behaviour, with discrepant pairs concentrating near the edges of the high-anisotropy areas as expected. The ‘core’ of the deformed material does not show discrepant splitting, as both phases show similar behaviour. Notably, for ppv 001 there is a region in the northeast which does not show the expected behaviour. We see a similar non-intuitive behaviour in path A (Figure 4b). Here, although some discrepant pairs straddle the edge of the slab for ppv 001, very few paths show this for any of the other models. Inferring the edges of anisotropic regions therefore must again be done with caution.

We also examine the raw difference in splitting intensity between SKS and SKKS at the same seismograms, $\Delta SI = SI_{\text{SKS}} - SI_{\text{SKKS}}$ (Figure 8). Measuring ΔSI is computationally simple, and hence holds the promise for automatic global mapping of D'' anisotropy. Comparing with the differential splitting predictions (Figures 4c, 6 and 7), it appears that the along-slab path B (Figure 8b) shows straightforward behaviour, where ΔSI deviates significantly from 0 where the slab is significantly anisotropic, either positively or negatively depending on the exact elastic structure in the model. This agrees well with the differential splitting interpretation. For path A, however (Figure 8a), a large negative ΔSI signal is present at the eastern end of most models, though this is not correlated to significant differential splitting (Figure 4c). Most models also show large ΔSI in the central northern part, but again this is not reflected in differential splitting. This suggests that although there is significant difference between the elastic structure experienced by the SKS and SKKS waves in these regions as they cross the edge of the anisotropic part of the slab, the shear wave splitting is not sufficiently coherent and clear to provide a strong signal. Nevertheless, these calculations suggest that a more global SKS–SKKS comparison holds promise for detecting regions where anisotropy changes rapidly.

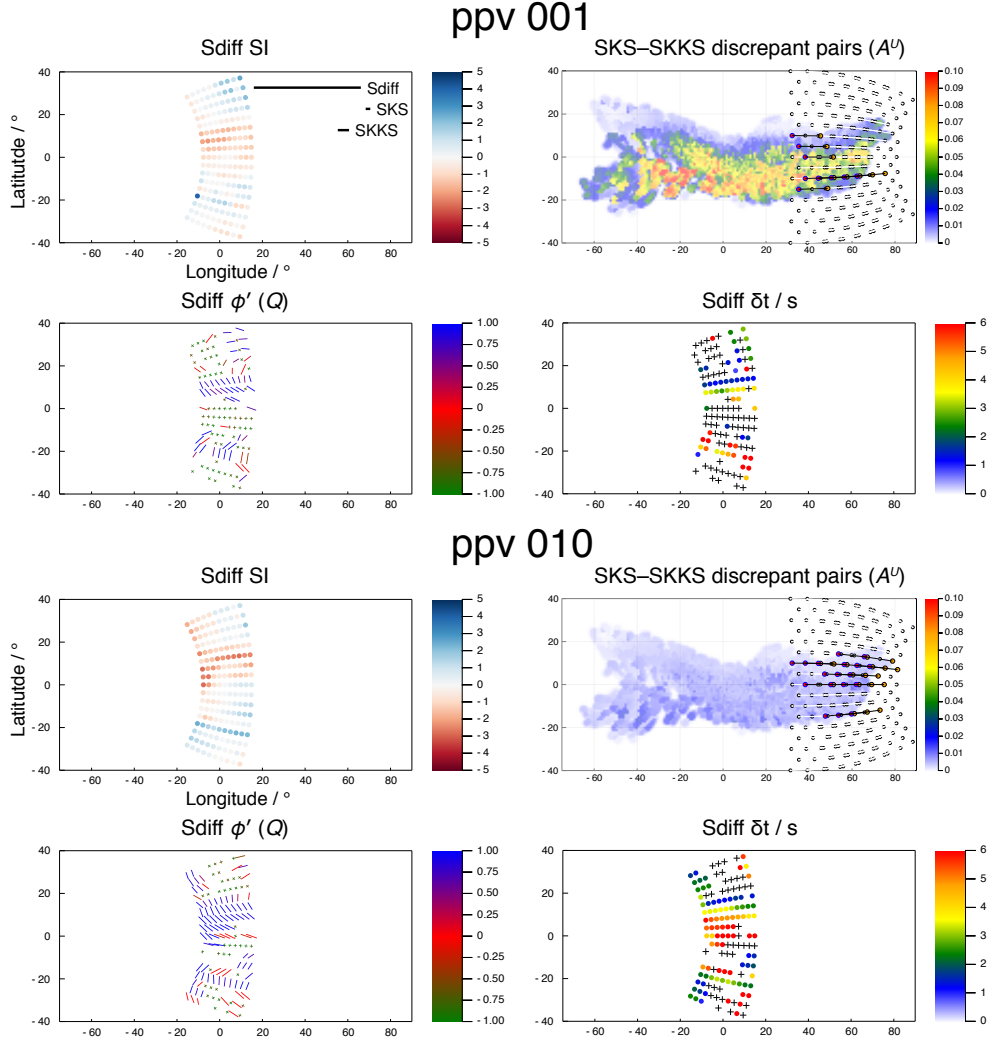


Figure 6. Shear-wave splitting results for the path ‘B’ (Table 1) and models ppv001 and ppv010. For each plasticity model, four panels show: (top left) the splitting intensity (Chevrot, 2000) of S_{diff} as colour; (bottom left) the ray-frame fast shear wave orientation of S_{diff} , coloured by the splitting quality measure Q (Wuestefeld et al., 2010); (bottom right) slow shear-wave delay time δt , coloured as per the scale bar; and (top right) pairs of discrepant SKS–SKKS splitting, where the red and orange circles show the core piercing point of SKKS and SKS, respectively, and white circles indicate no discrepant splitting; background colour shows strength of anisotropy as in Figure 4c. S_{diff} points are plotted at the end of the core-diffracted part of the path. The lengths of the ray paths of S_{diff} , SKS and SKKS in the lowermost 250 km of the mantle are shown in the SI panel for the ppv 001 case.

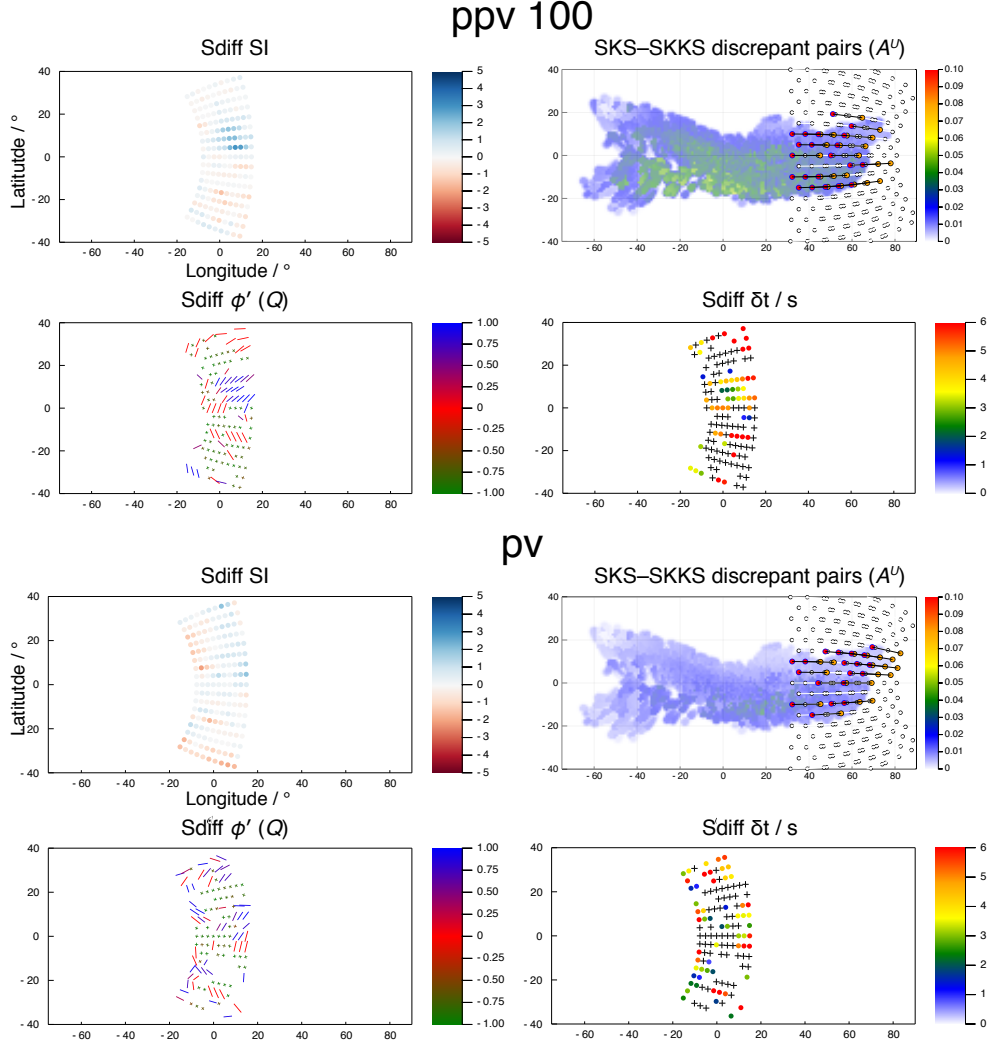


Figure 7. Shear-wave splitting results for the path ‘B’ (Table 1) and models ppv100 and pv. Features as for Figure 6.

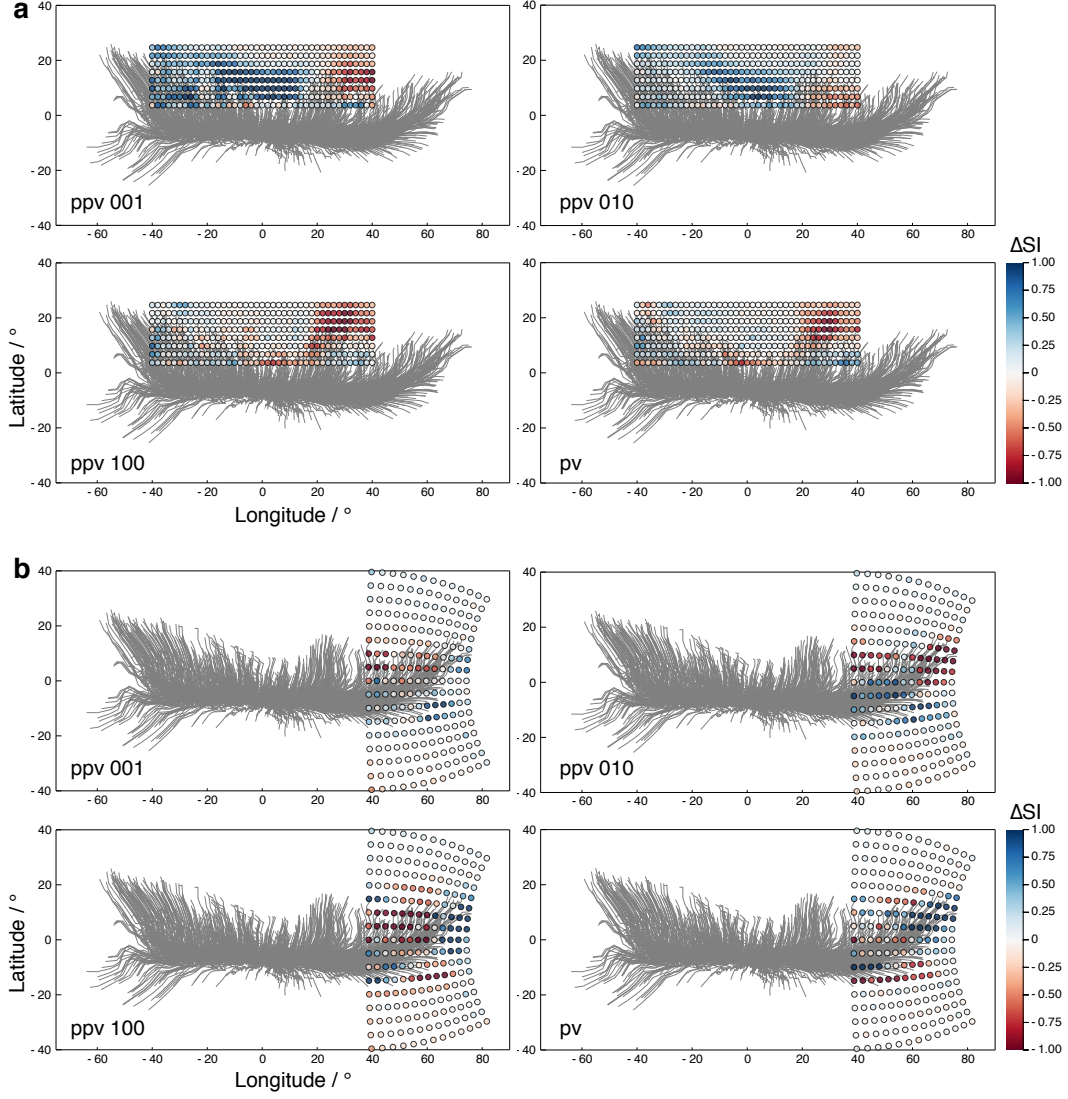


Figure 8. Difference in splitting intensity between SKS and SKKS, ΔSI , for (a) path A and (b) path B (Table 1). ΔSI is shown by colour according to the scale, lower right, at the midpoint between SKS and SKKS core–mantle boundary piercing points. Grey lines in the background show the path of tracers particles in the geodynamic model.

5 Limitations, advances, and the way forward

5.1 The inverse problem

The final goal of observing anisotropy in the lowermost mantle is, as the title of this chapter suggests, to map flow directions. We have discussed the forward model and the large number of assumptions required to create an anisotropic model and compare it to seismic observations. For most studies discussed in Section 4.1 the flow model was one of the prior assumptions and different potential compositions are explored; only the recent studies of Ford et al. (2015) and Creasy et al. (2017) locally interpret flow direction.

Results for a suite of candidate deformation mechanisms, like those in Figure 5, immediately make tempting a potentially circular line of reasoning: given an assumed flow model and the data, can we infer the deformation mechanism responsible for anisotropy? And with that improved estimate of deformation mechanism, can we then infer the flow field? As discussed, uncertainty as to the very cause of anisotropy in the lowermost mantle makes such reasoning perilous. It is also worth noting that if the rheology in geodynamic models is set in part based on observations of seismic anisotropy, and the assumption made of a particular deformation mechanism, then there is an added danger in the use of such dynamic models to then infer the mechanism of anisotropy.

Despite these problems, we can proceed with caution if we hold in mind that it is the *combination* of the flow model, deformation mechanism and mineral elasticity which is being tested against the data in each instance, not any one of these in isolation. Intuitively, varying any one of these might lead to an equally well-fitting set of synthetic observations when varying another.

Is finding the dominant mineral (or multi-phase system) and deformation systems creating lowermost mantle anisotropy the biggest hurdle in the way to mapping flow? If we constrain the main source of anisotropy, could we create a map of flow across the mantle? To do that, we would be interested in making a number of inverse steps (shown in Figure 3 by the white dashed arrows), each of which is non-linear and under-determined:

1. *Using the seismic observations to find the constrained parts of the seismic anisotropic tensor.* Constraints on the anisotropic tensor will always be limited by the propagation direction of the seismic phases used (Figure 2) and the azimuthal coverage, generally leaving large parts of the anisotropic tensor unconstrained, and reverting studies to assume symmetries (i.e. radial or azimuthal anisotropy). Additionally, the resulting anisotropic tensor would always reflect the effective elastic tensor that the seismic waves observed at long wavelengths, and could result from an entire suite of small-scaled heterogeneously (an)isotropic media (e.g., Backus, 1962; Capdeville & Cance, 2014; Fichtner et al., 2013). In this chapter we have frequently made the major assumption that the anisotropy of the effective tensor is due to underlying intrinsic anisotropy (CPO), and not caused by small-scale isotropic heterogeneity (SPO).
2. *Mapping from the effective anisotropic tensor to a set of textured minerals or a specific mineral with preferred orientation.* Accounting for the null-space in the elastic tensor, there would be no unique fit here and many assumptions on the mineral physics need to be made. One could not account for the entire suite of potential deformation mechanisms occurring, presence of other minerals and the related multi-phase deformation effects. With the assumption of a single dominant mineral and glide mechanism, the main imaged fast polarisation direction in the elastic tensor would be preferentially fit. There is no value in mapping the strength of the anisotropy into a degree of preferentially aligned minerals, as

the amplitudes of the effective elastic tensor will be underestimated (as shown by the synthetic results in Section 4.2).

3. *Mapping from textured minerals to potential deformation history and flow directions.* A single textured mineral can result from various deformation histories as it can both reflect the deformation it is undergoing, or fossilised deformation, which could be displaced and rotated. To uniquely constrain the flow model, many observations in different locations will have to be combined, as well as including other constraints, i.e. isotropic velocities, the gravity field, and past plate tectonic models.

While we choose to highlight the true inverse steps of this problem, this poses multiple layers of non-uniqueness, which makes a flow map for the lowermost mantle based on anisotropy appear unobtainable. For the foreseeable future, mapping mantle flow will have to rely on simplified relationships between fast polarisation directions and flow with understanding of the conditions under which these are valid. For the upper mantle, a simple relationship is posed as the fast axis of deformed olivine generally aligns with the flow direction, which has allowed interpretation of asthenospheric flow from anisotropy, although the validity of under volatile-rich conditions, e.g. in the mantle wedge above subduction zones, where observations also become more complex (see Becker and Lebedev, this volume). For the lowermost mantle, Cottaar et al. (2014) pose a similar relationship between horizontal fast direction and horizontal flow direction specifically for post-perovskite with dominant (001)-glide for a simple case of a slab spreading out on the CMB. Such a relationship should be tested statistically under many flow conditions, rotations, and deformations, and using full-waveform modelling. Tommasi et al. (2018) present a relationship of sub-parallel fast polarisation directions to the flow direction for post-perovskite with dominant (010)-glide and twinning for simple horizontal flow. Their study tests, not statistically but very systematically, the limitations of this relationship in corner flows and the ability of different seismic phases to detect these polarisation directions.

Creasy et al. (2019) pose a different question: with our current level of non-uniqueness in the interpretation, how many independent seismic observations do we need in a single location to interpret composition and flow? They show statistically that roughly 10 or more measurements of fast direction or reflection polarisations with various azimuths and incidence angles are needed to uniquely constrain the anisotropic tensor to make an interpretation with some confidence. It is challenging to find locations to which this can be applied due to available earthquake–station geometries.

Whilst it is unlikely that the mineralogical parameters we have discussed will be tightly constrained for some time, and similarly seismic data coverage will probably not improve vastly, it is conceivable that probabilistic approaches to inferring flow from anisotropy may enable progress by incorporating uncertainties in all the input parameters as in Figure 3 and retrieving an ensemble of acceptable flow histories. Such a model suite would however likely be a vast undertaking, requiring many millions of forward iterations, including geodynamic and full waveform modelling. This is unfeasible with the current combination of forward numerical methods and computational resources, but the future may bring this within our grasp.

5.2 Outlook

While mapping flow clearly remains an ambitious goal, current studies of anisotropy do provide new insights into the deepest mantle. Specifically, the goal to find the source of anisotropy reveals the potential importance of post-perovskite to be stable in the mantle, as bridgmanite might be too strong to cause texturing (Boioli et al., 2017) and ferropericlase, as the minor phase, might not deform coherently (Miyagi & Wenk, 2016). Observations of lateral changes in anisotropy could highlight where

post-perovskite is present, which relates to the temperature field and thus the convective patterns. A major step forward in understanding the role of post-perovskite would be to resolve its dominant deformation mechanisms. It remains to be seen if the latest theoretical calculations (e.g., Goryaeva et al., 2017) will converge with future experimental results.

Studies of anisotropy are also illuminating the nature of the LLSVP boundaries. From a seismological point of view, the claim that the radial anisotropy switches sign inside and outside the LLSVPs needs to be further tested for its robustness. Any relationship between the isotropic and anisotropic velocities in tomographic models could be an artefact (e.g., Chang et al., 2015). Local observations of splitting, however, have confirmed strong changes in anisotropy around the edges of the LLSVPs (e.g., Cottaar & Romanowicz, 2013; Wang & Wen, 2007; Lynner & Long, 2014). The nature of the LLSVPs poses major unanswered questions, and understanding the changing signatures of anisotropy can help resolve to what degree their boundaries represent a purely thermal or a thermo-chemical gradient. In the thermal case, change in anisotropy could be explained by a phase transition from post-perovskite to perovskite (Dobson et al., 2013) or by a change in flow direction, likely from horizontal outside to vertical within the LLSVPs or plumes (e.g. Wolf et al., 2019). In the case where LLSVPs represent thermo-chemical piles, the boundary could also be mechanical with separate convection inside and outside the piles (e.g., Garnero & McNamara, 2008). Currently, capturing all the variation in parameters which contribute to the development of anisotropy whilst correctly relating these to observations is computationally constrained. However, while we are far from producing a global flow map based on anisotropic variations, anisotropic studies play a role in answering these fundamental questions on the nature of the lowermost mantle. With the answers to these questions, flow can be more easily interpreted on the basis of mapped isotropic velocity variations.

Acknowledgments

The authors thank Andrew Walker for discussion and improvement of the manuscript, and acknowledge two anonymous reviewers and editor Hauke Marquardt for helpful and constructive comments. AN is supported by the Natural Environment Research Council (NERC grant reference number NE/R001154/1). SC is supported by the European Research Council (ERC) under the European Union’s Horizon 2020 research and innovation programme (grant agreement No. 804071 - ZoomDeep) and the Natural Environment Research Council (NERC grant reference number NE/R010862/1). Computations were performed on ARCHER.

References

- Ammann, M. W., Brodholt, J. P., Wookey, J., & Dobson, D. P. (2010). First-principles constraints on diffusion in lower-mantle minerals and a weak D'' layer. *Nature*, 465(7297), 462-465. doi: 10.1038/nature09052
- Amodeo, J., Carrez, P., Devincre, B., & Cordier, P. (2011). Multiscale modelling of MgO plasticity. *Acta Materialia*, 59(6), 2291–2301.
- Amodeo, J., Dancette, S., & Delannay, L. (2016). Atomistically-informed crystal plasticity in MgO polycrystals under pressure. *International Journal of Plasticity*, 82, 177–191.
- Antonangeli, D., Siebert, J., Aracne, C. M., Farber, D. L., Bosak, A., Hoesch, M., ... Badro, J. (2011). Spin crossover in ferropericlase at high pressure: A seismologically transparent transition? *Science*, 331(6013), 64–67.
- Auer, L., Boschi, L., Becker, T. W., Nissen-Meyer, T., & Giardini, D. (2014). Savani: A variable resolution whole-mantle model of anisotropic shear velocity vari-

- ations based on multiple data sets. *Journal Of Geophysical Research-Solid Earth*, 119(4), 3006-3034. doi: 10.1002/2013JB010773
- Backus, G. (1962). Long-wave elastic anisotropy produced by horizontal layering. *Journal Of Geophysical Research*, 67(11), 4427-4440. doi: 10.1029/JZ067i011p04427
- Beghein, C., Trampert, J., & van Heijst, H. J. (2006). Radial anisotropy in seismic reference models of the mantle. *Journal Of Geophysical Research-Solid Earth*, 111(B2), B02303. doi: 10.1029/2005JB003728
- Boioli, F., Carrez, P., Cordier, P., Devincere, B., Gouriet, K., Hirel, P., . . . Ritterbex, S. (2017). Pure climb creep mechanism drives flow in Earth's lower mantle. *Science Advances*, 3(3), e1601958.
- Borgeaud, A. F., Konishi, K., Kawai, K., & Geller, R. J. (2016). Finite frequency effects on apparent S-wave splitting in the D'' layer: Comparison between ray theory and full-wave synthetics. *Geophysical Journal International*, 207(1), 12-28.
- Boschi, L., & Dziewoński, A. (2000). Whole Earth tomography from delay times of P, PcP, and PKP phases: Lateral heterogeneities in the outer core or radial anisotropy in the mantle? *Journal Of Geophysical Research-Solid Earth*, 105(B6), 13675-13696.
- Capdeville, Y., & Cance, P. (2014). Residual homogenization for elastic wave propagation in complex media. *Geophysical Journal International*, 200(2), 986-999.
- Caracas, R., Mainprice, D., & Thomas, C. (2010). Is the spin transition in Fe²⁺-bearing perovskite visible in seismology? *Geophysical Research Letters*, 37, L13309. doi: 10.1029/2010GL043320
- Carrez, P., Ferré, D., & Cordier, P. (2009). Peierls-Nabarro modelling of dislocations in MgO from ambient pressure to 100 GPa. *Modelling And Simulation In Materials Science And Engineering*, 17(3), 035010. doi: 10.1088/0965-0393/17/3/035010
- Carrez, P., Goryaeva, A. M., & Cordier, P. (2017). Prediction of mechanical twinning in magnesium silicate post-perovskite. *Scientific reports*, 7(1), 17640.
- Chandler, B., Yuan, K., Li, M., Cottaar, S., Romanowicz, B., Tomé, C., & Wenk, H. (2018). A refined approach to model anisotropy in the lowermost mantle. In *Iop conference series: Materials science and engineering* (Vol. 375, p. 012002).
- Chang, S.-J., Ferreira, A. M. G., Ritsema, J., van Heijst, H. J., & Woodhouse, J. H. (2015). Joint inversion for global isotropic and radially anisotropic mantle structure including crustal thickness perturbations. *Journal of Geophysical Research: Solid Earth*, 120(6), 4278-4300. doi: 10.1002/2014JB011824
- Chevrot, S. (2000). Multichannel analysis of shear wave splitting. *Journal Of Geophysical Research-Solid Earth*, 105(B9), 21579-21590.
- Cobden, L., & Thomas, C. (2013). The origin of D'' reflections: A systematic study of seismic array data sets. *Geophysical Journal International*, 194(2), 1091-1118.
- Cobden, L., Thomas, C., & Trampert, J. (2015). Seismic detection of post-perovskite inside the Earth. In *The earth's heterogeneous mantle* (pp. 391-440). Springer.
- Cordier, P., Amodeo, J., & Carrez, P. (2012). Modelling the rheology of MgO under Earth's mantle pressure, temperature and strain rates. *Nature*, 481(7380), 177-180. doi: 10.1038/nature10687
- Cottaar, S., & Lekić, V. (2016). Morphology of seismically slow lower-mantle structures. *Geophys. J. Int.*, 207(2), 1122-1136. doi: 10.1093/gji/ggw324
- Cottaar, S., Li, M., McNamara, A. K., Romanowicz, B., & Wenk, H.-R. (2014). Synthetic seismic anisotropy models within a slab impinging on the core-mantle boundary. *Geophysical Journal International*, 199(1), 164-177. doi: 10.1093/gji/ggu244
- Cottaar, S., & Romanowicz, B. (2013). Observations of changing anisotropy across the southern margin of the African LLSVP. *Geophysical Journal International*,

- 195(2), 1184-1195. doi: 10.1093/gji/ggt285
- Creasy, N., Long, M. D., & Ford, H. A. (2017). Deformation in the lowermost mantle beneath Australia from observations and models of seismic anisotropy. *Journal of Geophysical Research: Solid Earth*, 122(7), 5243-5267. doi: 10.1002/2016JB013901
- Creasy, N., Pisconti, A., Long, M. D., Thomas, C., & Wookey, J. (2019). Constraining lowermost mantle anisotropy with body waves: a synthetic modelling study. *Geophysical Journal International*, 217(2), 766-783.
- de Wit, R., & Trampert, J. (2015). Robust constraints on average radial lower mantle anisotropy and consequences for composition and texture. *Earth and Planetary Science Letters*, 429, 101-109. doi: 10.1016/j.epsl.2015.07.057
- Deng, J., Long, M. D., Creasy, N., Wagner, L., Beck, S., Zandt, G., ... Minaya, E. (2017). Lowermost mantle anisotropy near the eastern edge of the Pacific LLSVP: constraints from SKS-SKKS splitting intensity measurements. *Geophysical Journal International*, 210(2), 774-786.
- Dobson, D. P., Lindsay-Scott, A., Hunt, S., Bailey, E., Wood, I., Brodholt, J. P., ... Wheeler, J. (2019). Anisotropic diffusion creep in postperovskite provides a new model for deformation at the core-mantle boundary. *Proceedings of the National Academic of Sciences*, 116(52), 26389-26393.
- Dobson, D. P., Miyajima, N., Nestola, F., Alvaro, M., Casati, N., Liebske, C., ... Walker, A. M. (2013). Strong inheritance of texture between perovskite and post-perovskite in the D'' layer. *Nature Geoscience*, 6(7), 575-578. doi: 10.1038/ngeo1844
- Duan, Y., Sun, N., Wang, S., Li, X., Guo, X., Ni, H., ... Mao, Z. (2018). Phase stability and thermal equation of state of δ -AlOOH: Implication for water transportation to the Deep Lower Mantle. *Earth and Planetary Science Letters*, 494, 92-98. doi: 10.1016/j.epsl.2018.05.003
- Ferré, D., Carrez, P., & Cordier, P. (2007). First principles determination of dislocations properties of MgSiO_3 perovskite at 30 GPa based on the Peierls-Nabarro model. *Physics of the Earth and Planetary Interiors*, 163(1-4), 283-291.
- Ferré, D., Cordier, P., & Carrez, P. (2009). Dislocation modeling in calcium silicate perovskite based on the Peierls-Nabarro model. *American Mineralogist*, 94(1), 135-142. doi: 10.2138/am.2009.3003
- Ferreira, A. M. G., Faccenda, M., Sturgeon, W., Chang, S.-J., & Schardong, L. (2019). Ubiquitous lower-mantle anisotropy beneath subduction zones. *Nature Geoscience*, 12(4), 301. doi: 10.1038/s41561-019-0325-7
- Ferreira, A. M. G., Woodhouse, J. H., Visser, K., & Trampert, J. (2010). On the robustness of global radially anisotropic surface wave tomography. *Journal Of Geophysical Research-Solid Earth*, 115, B04313. doi: 10.1029/2009JB006716
- Fichtner, A., Kennett, B. L., & Trampert, J. (2013). Separating intrinsic and apparent anisotropy. *Physics of the Earth and Planetary Interiors*, 219, 11-20.
- Finkelstein, G. J., Jackson, J. M., Said, A., Alatas, A., Leu, B. M., Sturhahn, W., & Toellner, T. S. (2018). Strongly anisotropic magnesiowüstite in Earth's lower mantle. *Journal of Geophysical Research: Solid Earth*, 123(6), 4740-4750.
- Ford, H. A., & Long, M. D. (2015). A regional test of global models for flow, rheology, and seismic anisotropy at the base of the mantle. *Physics of the Earth and Planetary Interiors*, 245, 71-75. doi: 10.1016/j.pepi.2015.05.004
- Ford, H. A., Long, M. D., He, X., & Lynner, C. (2015). Lowermost mantle flow at the eastern edge of the African Large Low Shear Velocity Province. *Earth and Planetary Science Letters*, 420, 12-22. doi: 10.1016/j.epsl.2015.03.029
- French, S. W., & Romanowicz, B. (2015). Broad plumes rooted at the base of the Earth's mantle beneath major hotspots. *Nature*, 525(7567), 95-99. doi: 10.1038/nature14876
- Fu, S., Yang, J., Tsujino, N., Okuchi, T., Purevjav, N., & Lin, J.-F. (2019). Single-

- crystal elasticity of (Al, Fe)-bearing bridgmanite and seismic shear wave radial anisotropy at the topmost lower mantle. *Earth and Planetary Science Letters*, *518*, 116–126.
- Garnero, E. J., & Lay, T. (1997). Lateral variations in lowermost mantle shear wave anisotropy beneath the north Pacific and Alaska. *Journal Of Geophysical Research-Solid Earth*, *102*(B4), 8121–8135. doi: 10.1029/96JB03830
- Garnero, E. J., Maupin, V., Lay, T., & Fouch, M. J. (2004). Variable azimuthal anisotropy in Earth’s lowermost mantle. *Science*, *306*(5694), 259–261. doi: 10.1126/science.1103411
- Garnero, E. J., & McNamara, A. K. (2008). Structure and dynamics of Earth’s lower mantle. *Science*, *320*(5876), 626–628. doi: 10.1126/science.1148028
- Garnero, E. J., McNamara, A. K., & Shim, S.-H. (2016). Continent-sized anomalous zones with low seismic velocity at the base of Earth’s mantle. *Nature Geoscience*, *9*(7), 481–489. doi: 10.1038/ngeo2733
- Garnero, E. J., Revenaugh, J., Williams, Q., Lay, T., & Kellogg, L. (1998). Ultralow velocity zone at the core–mantle boundary. In M. Gurnis, M. E. Wyssession, E. Knittle, & B. A. Buffett (Eds.), *The Core–Mantle Boundary Region* (pp. 319–334). Washington, D.C., USA: American Geophysical Union.
- Gialampouki, M. A., Xu, S., & Morgan, D. (2018). Iron valence and partitioning between post-perovskite and ferropericlase in the Earth’s lowermost mantle. *Physics of the Earth and Planetary Interiors*, *282*, 110–116. doi: 10.1016/j.pepi.2018.06.005
- Girard, J., Amulele, G., Farla, R., Mohiuddin, A., & Karato, S.-i. (2016). Shear deformation of bridgmanite and magnesiowüstite aggregates at lower mantle conditions. *Science*, *351*(6269), 144–147. doi: 10.1126/science.aad3113
- Girard, J., Chen, J., & Raterron, P. (2012). Deformation of periclase single crystals at high pressure and temperature: Quantification of the effect of pressure on slip-system activities. *Journal of Applied Physics*, *111*(11), 112607.
- Goryaeva, A. M., Carrez, P., & Cordier, P. (2015). Modeling defects and plasticity in MgSiO₃ post-perovskite: Part 2—Screw and edge [100] dislocations. *Physics and chemistry of minerals*, *42*(10), 793–803.
- Goryaeva, A. M., Carrez, P., & Cordier, P. (2016). Low viscosity and high attenuation in MgSiO₃ post-perovskite inferred from atomic-scale calculations. *Scientific reports*, *6*, 34771.
- Goryaeva, A. M., Carrez, P., & Cordier, P. (2017). Modeling defects and plasticity in MgSiO₃ post-perovskite: Part 3—Screw and edge [001] dislocations. *Physics and Chemistry of Minerals*, *44*(7), 521–533.
- Grund, M., & Ritter, J. R. (2019). Widespread seismic anisotropy in Earth’s lowermost mantle beneath the Atlantic and Siberia. *Geology*, *47*(2), 123–126.
- Hall, S. A., Kendall, J.-M., & Van der Baan, M. (2004). Some comments on the effects of lower-mantle anisotropy on SKS and SKKS phases. *Physics of The Earth and Planetary Interiors*, *146*(3–4), 469–481. doi: 10.1016/j.pepi.2004.05.002
- Hernlund, J., Thomas, C., & Tackley, P. J. (2005). A doubling of the post-perovskite phase boundary and structure of the Earth’s lowermost mantle. *Nature*, *434*(7035), 882–886. doi: 10.1038/nature03472
- Hirose, K., Nagaya, Y., Merkel, S., & Ohishi, Y. (2010). Deformation of MnGeO₃ post-perovskite at lower mantle pressure and temperature. *Geophysical Research Letters*, *37*(L20302), 1–5. doi: 10.1029/2010GL044977
- Hirose, K., Wentzcovitch, R., Yuen, D., & Lay, T. (2015). Mineralogy of the deep mantle - The post-perovskite phase and its geophysical significance. *Treatise on Geophysics*, 85–115.
- Hu, Q., Kim, D. Y., Yang, W., Yang, L., Meng, Y., Zhang, L., & Mao, H.-K. (2016). FeO₂ and FeOOH under deep lower-mantle conditions and Earth’s oxygen–hydrogen cycles. *Nature*, *534*(7606), 241–244. doi: 10.1038/nature18018

- Hunt, S. A., Walker, A. M., & Mariani, E. (2016). In-situ measurement of texture development rate in CaIrO_3 post-perovskite. *Physics of the Earth and Planetary Interiors*. doi: 10.1016/j.pepi.2016.05.007
- Hunt, S. A., Weidner, D. J., Li, L., Wang, L., Walte, N. P., Brodholt, J. P., & Dobson, D. P. (2009). Weakening of calcium iridate during its transformation from perovskite to post-perovskite. *Nature Geoscience*, 2(11), 794-797. doi: 10.1038/NNGEO663
- Iitaka, T., Hirose, K., Kawamura, K., & Murakami, M. (2004). The elasticity of the MgSiO_3 post-perovskite phase in the Earth's lowermost mantle. *Nature*, 430(6998), 442-445. doi: 10.1038/nature02702
- Jackson, J. M., Sinogeikin, S. V., Jacobsen, S. D., Reichmann, H. J., Mackwell, S. J., & Bass, J. D. (2006). Single-crystal elasticity and sound velocities of $(\text{Mg}_{0.94}\text{Fe}_{0.06})\text{O}$ ferropericlasite to 20 GPa. *Journal of Geophysical Research: Solid Earth*, 111(B9).
- Kaercher, P., Miyagi, L., Kanitpanyacharoen, W., Zepeda-Alarcon, E., Wang, Y., Parkinson, D., ... Wenk, H. (2016). Two-phase deformation of lower mantle mineral analogs. *Earth and Planetary Science Letters*, 456, 134-145. doi: 10.1016/j.epsl.2016.09.030
- Karato, S.-i. (1998). Some remarks on the origin of seismic anisotropy in the D'' layer. *Earth Planets Space*, 50, 1019-1028.
- Karki, B., Stixrude, L., & Crain, J. (1997). Ab initio elasticity of three high-pressure polymorphs of silica. *Geophysical Research Letters*, 24(24), 3269-3272. doi: 10.1029/97GL53196
- Karki, B., Wentzcovitch, R., de Gironcoli, S., & Baroni, S. (2000). High-pressure lattice dynamics and thermoelasticity of MgO . *Physical Review B*, 61(13), 8793.
- Kawai, K., & Geller, R. J. (2010). The vertical flow in the lowermost mantle beneath the Pacific from inversion of seismic waveforms for anisotropic structure. *Earth and Planetary Science Letters*, 297(1-2), 190-198. doi: 10.1016/j.epsl.2010.05.037
- Kawakatsu, H. (2015). A new fifth parameter for transverse isotropy. *Geophysical Journal International*, 204(1), 682-685.
- Kendall, J.-M., & Silver, P. G. (1996). Constraints from seismic anisotropy on the nature of the lowermost mantle. *Nature*, 381(6581), 409-412. doi: 10.1038/381409a0
- Kendall, J.-M., & Silver, P. G. (1998). Investigating causes of D'' anisotropy. In *The core-mantle boundary region* (p. 97-118). American Geophysical Union.
- Kennett, B. L. N., Engdahl, E., & Buland, R. (1995). Constraints on seismic velocities in the Earth from travel-times. *Geophysical Journal International*, 122(1), 108-124. doi: 10.1111/j.1365-246X.1995.tb03540.x
- Koelemeijer, P., Schuberth, B., Davies, D., Deuss, A., & Ritsema, J. (2018). Constraints on the presence of post-perovskite in Earth's lowermost mantle from tomographic-geodynamic model comparisons. *Earth and Planetary Science Letters*, 494, 226-238. doi: 10.1016/j.epsl.2018.04.056
- Koelemeijer, P. J., Deuss, A., & Trampert, J. (2012). Normal mode sensitivity to earth's D'' layer and topography on the core-mantle boundary: what we can and cannot see. *Geophysical Journal International*, 190(1), 553-568. doi: 10.1111/j.1365-246X.2012.05499.x
- Komatitsch, D., & Tromp, J. (2002). Spectral-element simulations of global seismic wave propagation - I. Validation. *Geophysical Journal International*, 149(2), 390-412.
- Komatitsch, D., Tsuboi, S., Ji, C., & Tromp, J. (2003). A 14.6 billion degrees of freedom, 5 teraflops, 2.5 terabyte earthquake simulation on the Earth Simulator. *Proceedings of the ACM/IEEE SC2003 Conference (SC'03)*, 1-8. doi: 10.1145/1048935.1050155

- Komatitsch, D., Vinnik, L. P., & Chevrot, S. (2010). SHdiff-SVdiff splitting in an isotropic Earth. *Journal Of Geophysical Research-Solid Earth*, *115*, B07312. doi: 10.1029/2009JB006795
- Krischer, L., Megies, T., Barsch, R., Beyreuther, M., Lecocq, T., Caudron, C., & Wassermann, J. (2015). Obspy: A bridge for seismology into the scientific Python ecosystem. *Computational Science & Discovery*, *8*(1), 014003.
- Lay, T., & Young, C. (1991). Analysis of seismic SV waves in the core's penumbra. *Geophysical Research Letters*, *18*(8), 1373-1376. doi: 10.1029/91GL01691
- Lebensohn, R., & Tomé, C. (1993). A self-consistent anisotropic approach for the simulation of plastic-deformation and texture development of polycrystals—application to zirconium alloys. *Acta Metallurgica Et Materialia*, *41*(9), 2611–2624. doi: 10.1016/0956-7151(93)90130-K
- Lekić, V., Cottaar, S., Dziewoński, A., & Romanowicz, B. (2012). Cluster analysis of global lower mantle tomography: A new class of structure and implications for chemical heterogeneity. *Earth and Planetary Science Letters*, *357-358*, 68-77. doi: 10.1016/j.epsl.2012.09.014
- Li, L., Brodholt, J. P., Stackhouse, S., Weidner, D. J., Alfredsson, M., & Price, G. D. (2005). Elasticity of (Mg, Fe)(Si, Al)O₃-perovskite at high pressure. *Earth and Planetary Science Letters*, *240*(2), 529–536.
- Li, L., Weidner, D. J., Brodholt, J. P., Alfé, D., Price, G. D., Caracas, R., & Wentzcovitch, R. M. (2006). Elasticity of CaSiO₃ perovskite at high pressure and high temperature. *Physics of The Earth and Planetary Interiors*, *155*(3-4), 249-259. doi: 10.1016/j.pepi.2005.12.006
- Lin, J.-F., Wenk, H.-R., Voltolini, M., Speziale, S., Shu, J., & Duffy, T. S. (2009). Deformation of lower-mantle ferropericlasite (Mg, Fe)O across the electronic spin transition. *Physics and Chemistry of Minerals*, *36*(10), 585.
- Long, M. (2009). Complex anisotropy in D'' beneath the eastern pacific from SKS-SKKS splitting discrepancies. *Earth and Planetary Science Letters*, *283*(1-4), 181-189. doi: 10.1016/j.epsl.2009.04.019
- Long, M. D., & Lynner, C. (2015). Seismic anisotropy in the lowermost mantle near the Perm Anomaly. *Geophysical Research Letters*, *42*(17), 7073-7080. doi: 10.1002/2015GL065506
- Lynner, C., & Long, M. D. (2014). Lowermost mantle anisotropy and deformation along the boundary of the African LLSVP. *Geophysical Research Letters*, *41*(10), 3447-3454. doi: 10.1002/2014GL059875
- Madi, K., Forest, S., Cordier, P., & Boussuge, M. (2005). Numerical study of creep in two-phase aggregates with a large rheology contrast: Implications for the lower mantle. *Earth and Planetary Science Letters*, *237*(1-2), 223–238.
- Mainprice, D. (2007). Seismic anisotropy of the deep Earth from a mineral and rock physics perspective. In *Treatise on Geophysics* (p. 437-491). Elsevier. doi: 10.1016/B978-044452748-6.00045-6
- Mainprice, D., Tommasi, A., Ferré, D., Carrez, P., & Cordier, P. (2008). Predicted glide systems and crystal preferred orientations of polycrystalline silicate Mg-Perovskite at high pressure: Implications for the seismic anisotropy in the lower mantle. *Earth and Planetary Science Letters*, *271*(1-4), 135-144. doi: 10.1016/j.epsl.2008.03.058
- Mancinelli, N. J., & Shearer, P. M. (2013). Reconciling discrepancies among estimates of small-scale mantle heterogeneity from PKP precursors. *Geophysical Journal International*, *195*(3), 1721–1729.
- Mao, W. L., Meng, Y., & Mao, H. (2010). Elastic anisotropy of ferromagnesian post-perovskite in Earth's D'' layer. *Physics of The Earth and Planetary Interiors*, *180*(3-4), 203-208. doi: 10.1016/j.pepi.2009.10.013
- Marquardt, H., Speziale, S., Reichmann, H. J., Frost, D. J., & Schilling, F. R. (2009). Single-crystal elasticity of (Mg_{0.9}Fe_{0.1})O to 81 GPa. *Earth and Plane-*

- tary Science Letters*, 287(3-4), 345-352. doi: 10.1016/j.epsl.2009.08.017
- Matzel, E., Sen, M., & Grand, S. (1996). Evidence for anisotropy in the deep mantle beneath Alaska. *Geophysical Research Letters*, 23(18), 2417-2420. doi: 10.1029/96GL02186
- Maupin, V. (1994). On the possibility of anisotropy in the D'' layer as inferred from the polarization of diffracted S waves. *Physics of The Earth and Planetary Interiors*, 87(1-2), 1-32. doi: 10.1016/0031-9201(94)90019-1
- Maupin, V., Garnero, E. J., Lay, T., & Fouch, M. J. (2005). Azimuthal anisotropy in the D'' layer beneath the Caribbean. *Journal Of Geophysical Research-Solid Earth*, 110(B8), B08301. doi: 10.1029/2004JB003506
- McDonough, W., & Sun, S. (1995). The composition of the Earth. *Chemical Geology*, 120(3-4), 223-253.
- Merkel, S., McNamara, A. K., Kubo, A., Speziale, S., Miyagi, L., Meng, Y., ... Wenk, H.-R. (2007). Deformation of (Mg,Fe)SiO₃ post-perovskite and D'' anisotropy. *Science*, 316(5832), 1729-1732. doi: 10.1126/science.1140609
- Merkel, S., Wenk, H.-R., Shu, J., Shen, G., Gillet, P., Mao, H., & Hemley, R. (2002). Deformation of polycrystalline MgO at pressures of the lower mantle. *Journal Of Geophysical Research-Solid Earth*, 107(B11), 2271. doi: 10.1029/2001JB000920
- Miyagi, L. (2020). Experimental deformation of lower mantle rocks and minerals. In H. Marquardt, M. Ballmer, S. Cottaar, & J. Konter (Eds.), *Mantle convection and surface expressions*. American Geophysical Union.
- Miyagi, L., Kanitpanyacharoen, W., Kaercher, P., Lee, K. K. M., & Wenk, H.-R. (2010). Slip systems in MgSiO₃ post-perovskite: Implications for D'' anisotropy. *Science*, 329(5999), 1639-1641. doi: 10.1126/science.1192465
- Miyagi, L., Kanitpanyacharoen, W., Stackhouse, S., Militzer, B., & Wenk, H.-R. (2011). The enigma of post-perovskite anisotropy: Deformation versus transformation textures. *Physics And Chemistry Of Minerals*, 38(9), 665-678. doi: 10.1007/s00269-011-0439-y
- Miyagi, L., Merkel, S., Yagi, T., Sata, N., Ohishi, Y., & Wenk, H.-R. (2009). Diamond anvil cell deformation of CaSiO₃ perovskite up to 49 GPa. *Physics of the Earth and Planetary Interiors*, 174(1-4), 159-164. doi: 10.1016/j.pepi.2008.05.018
- Miyagi, L., & Wenk, H.-R. (2016). Texture development and slip systems in bridgmanite and bridgmanite + ferropericlasite aggregates. *Physics and Chemistry of Minerals*, 43(8), 597-613.
- Moulik, P., & Ekstrom, G. (2014). An anisotropic shear velocity model of the Earth's mantle using normal modes, body waves, surface waves and long-period waveforms. *Geophys. J. Int.*, 199(3), 1713-1738. doi: 10.1093/gji/ggu356
- Murakami, M., Hirose, K., Kawamura, K., Sata, N., & Ohishi, Y. (2004). Post-perovskite phase transition in MgSiO₃. *Science*, 304(5672), 855-858. doi: 10.1126/science.1095932
- Nakagawa, T., & Tackley, P. J. (2011). Effects of low-viscosity post-perovskite on thermo-chemical mantle convection in a 3-D spherical shell. *Geophysical research letters*, 38(4).
- Nisr, C., Ribárik, G., Ungar, T., Vaughan, G. B. M., Cordier, P., & Merkel, S. (2012). High resolution three-dimensional X-ray diffraction study of dislocations in grains of MgGeO₃ post-perovskite at 90 GPa. *Journal Of Geophysical Research*, 117(B3), B03201. doi: 10.1029/2011JB008401
- Niu, F., & Perez, A. (2004). Seismic anisotropy in the lower mantle: A comparison of waveform splitting of SKS and SKKS. *Geophysical Research Letters*, 31(24), L24612. doi: 10.1029/2004GL021196
- Niwa, K., Miyajima, N., Seto, Y., Ohgushi, K., Gotou, H., & Yagi, T. (2012). In situ observation of shear stress-induced perovskite to post-perovskite phase transition in CaIrO₃ and the development of its deformation texture in a diamond-anvil cell

- up to 30 GPa. *Physics of The Earth and Planetary Interiors*, 194-195(C), 10-17. doi: 10.1016/j.pepi.2012.01.007
- Nowacki, A., Walker, A. M., Wookey, J., & Kendall, J.-M. (2013). Evaluating post-perovskite as a cause of D'' anisotropy in regions of palaeosubduction. *Geophysical Journal International*, 192(3), 1085-1090. doi: 10.1093/gji/ggs068
- Nowacki, A., & Wookey, J. (2016). The limits of ray theory when measuring shear wave splitting in the lowermost mantle with ScS waves. *Geophysical Journal International*, 207, 1573-1583. doi: 10.1093/gji/ggw358
- Nowacki, A., Wookey, J., & Kendall, J.-M. (2010). Deformation of the lowermost mantle from seismic anisotropy. *Nature*, 467(7319), 1091-1095. doi: 10.1038/nature09507
- Nowacki, A., Wookey, J., & Kendall, J.-M. (2011). New advances in using seismic anisotropy, mineral physics and geodynamics to understand deformation in the lowermost mantle. *Journal of Geodynamics*, 52(3-4), 205-228. doi: 10.1016/j.jog.2011.04.003
- Oganov, A., Brodholt, J. P., & Price, G. D. (2001). The elastic constants of MgSiO₃ perovskite at pressures and temperatures of the Earth's mantle. *Nature*, 411(6840), 934-937. doi: 10.1038/35082048
- Oganov, A., & Ono, S. (2004). Theoretical and experimental evidence for a post-perovskite phase of MgSiO₃ in Earth's D'' layer. *Nature*, 430(6998), 445-448. doi: 10.1038/nature02701
- Pamato, M. G., Myhill, R., Boffa Ballaran, T., Frost, D. J., Heidelbach, F., & Miyajima, N. (2015). Lower-mantle water reservoir implied by the extreme stability of a hydrous aluminosilicate. *Nature Geoscience*, 8(1), 75-79. doi: 10.1038/ngeo2306
- Panero, W. R., & Caracas, R. (2017). Stability of phase H in the MgSiO₄H₂-AlOOH-SiO₂ system. *Earth and Planetary Science Letters*, 463, 171-177. doi: 10.1016/j.epsl.2017.01.033
- Panning, M., Lekić, V., & Romanowicz, B. (2010). Importance of crustal corrections in the development of a new global model of radial anisotropy. *Journal Of Geophysical Research-Solid Earth*, 115, B12325. doi: 10.1029/2010JB007520
- Parisi, L., Ferreira, A. M. G., & Ritsema, J. (2018). Apparent splitting of S waves propagating through an isotropic lowermost mantle. *Journal of Geophysical Research: Solid Earth*, 123(5), 3909-3922. doi: 10.1002/2017JB014394
- Pisconti, A., Thomas, C., & Wookey, J. (2019). Discriminating between causes of D'' anisotropy using reflections and splitting measurements for a single path. *Journal of Geophysical Research: Solid Earth*. doi: 10.1029/2018JB016993
- Ranganathan, S. I., & Ostoya-Starzewski, M. (2008). Universal elastic anisotropy index. *Physical Review Letters*, 101(5), 055504. doi: 10.1103/PhysRevLett.101.055504
- Realì, R., Van Orman, J. A., Pigott, J. S., Jackson, J. M., Boioli, F., Carrez, P., & Cordier, P. (2019). The role of diffusion-driven pure climb creep on the rheology of bridgmanite under lower mantle conditions. *Scientific reports*, 9(1), 2053.
- Reiss, M., Long, M., & Creasy, N. (2019). Lowermost mantle anisotropy beneath Africa from differential SKS-SKKS shear-wave splitting. *Journal of Geophysical Research: Solid Earth*. doi: 10.1029/2018JB017160
- Romanowicz, B., & Wenk, H.-R. (2017). Anisotropy in the deep Earth. *Physics of the Earth and Planetary Interiors*, 269, 58-90. doi: 10.1016/j.pepi.2017.05.005
- Silver, P. G., & Chan, W. W. (1991). Shear-wave splitting and subcontinental mantle deformation. *Journal Of Geophysical Research-Solid Earth*, 96(B10), 16429-16454. doi: 10.1029/91JB00899
- Simmons, N. A., Forte, A. M., & Grand, S. (2009). Joint seismic, geodynamic and mineral physical constraints on three-dimensional mantle heterogeneity: Implications for the relative importance of thermal versus compositional

- heterogeneity. *Geophysical Journal International*, 177(3), 1284-1304. doi: 10.1111/j.1365-246X.2009.04133.x
- Soldati, G., Boschi, L., & Piersanti, A. (2003). Outer core density heterogeneity and the discrepancy between PKP and PcP travel time observations. *Geophysical Research Letters*, 30(4), 1190. doi: 10.1029/2002GL016647
- Stackhouse, S., Brodholt, J. P., & Price, G. D. (2005). High temperature elastic anisotropy of the perovskite and post-perovskite Al_2O_3 . *Geophysical Research Letters*, 32(13), L13305. doi: 10.1029/2005GL023163
- Stackhouse, S., Brodholt, J. P., Wookey, J., Kendall, J.-M., & Price, G. D. (2005). The effect of temperature on the seismic anisotropy of the perovskite and post-perovskite polymorphs of MgSiO_3 . *Earth and Planetary Science Letters*, 230(1-2), 1-10. doi: 10.1016/j.epsl.2004.11.021
- Sun, N., Shi, W., Mao, Z., Zhou, C., & Prakapenka, V. B. (2019). High pressure-temperature study on the thermal equations of state of seifertite and CaCl_2 -type SiO_2 . *Journal of Geophysical Research: Solid Earth*, 124(12), 12620–12630. doi: 10.1029/2019JB017853
- Tesoniero, A., Cammarano, F., & Boschi, L. (2016). S-to-P heterogeneity ratio in the lower mantle and thermo-chemical implications. *Geochemistry, Geophysics, Geosystems*, 17(7), 2522-2538. doi: 10.1002/2016GC006293
- Thomas, C., Wookey, J., Brodholt, J. P., & Fieseler, T. (2011). Anisotropy as cause for polarity reversals of D'' reflections. *Earth and Planetary Science Letters*, 307(3-4), 369-376. doi: 10.1016/j.epsl.2011.05.011
- Thomas, C., Wookey, J., & Simpson, M. (2007). D'' anisotropy beneath Southeast Asia. *Geophysical Research Letters*, 34(4), L04301. doi: 10.1029/2006GL028965
- Thomson, A. R., Crichton, W. A., Brodholt, J. P., Wood, I. G., Siersch, N. C., Muir, J. M. R., . . . Hunt, S. A. (2019). Seismic velocities of CaSiO_3 perovskite can explain LLSVPs in Earth's lower mantle. *Nature*, 572(7771), 643–647. doi: 10.1038/s41586-019-1483-x
- Tommasi, A., Goryaeva, A., Carrez, P., Cordier, P., & Mainprice, D. (2018). Deformation, crystal preferred orientations, and seismic anisotropy in the Earth's D'' layer. *Earth and Planetary Science Letters*, 492, 35-46. doi: 10.1016/j.epsl.2018.03.032
- Tsuchiya, T., Tsuchiya, J., Umemoto, K., & Wentzcovitch, R. M. (2004). Phase transition in MgSiO_3 perovskite in the earth's lower mantle. *Earth and Planetary Science Letters*, 224(3-4), 241-248. doi: 10.1016/j.epsl.2004.05.017
- Tsujino, N., Nishihara, Y., Yamazaki, D., Seto, Y., Higo, Y., & Takahashi, E. (2016). Mantle dynamics inferred from the crystallographic preferred orientation of bridgmanite. *Nature*, 539(7627), 81-84. doi: 10.1038/nature19777
- Vinnik, L. P., Breger, L., & Romanowicz, B. (1998). Anisotropic structures at the base of the Earth's mantle. *Nature*, 393(6685), 564-567. doi: 10.1038/31208
- Walker, A. M., Carrez, P., & Cordier, P. (2010). Atomic-scale models of dislocation cores in minerals: Progress and prospects. *Mineralogical Magazine*, 74(3), 381-413. doi: 10.1180/minmag.2010.074.3.381
- Walker, A. M., Dobson, D. P., Wookey, J., Nowacki, A., & Forte, A. M. (2018). The anisotropic signal of topotaxy during phase transitions in D'' . *Physics of the Earth and Planetary Interiors*, 276, 159-171. doi: 10.1016/j.pepi.2017.05.013
- Walker, A. M., Forte, A. M., Wookey, J., Nowacki, A., & Kendall, J.-M. (2011). Elastic anisotropy of D'' predicted from global models of mantle flow. *Geochemistry Geophysics Geosystems*, 12(10), Q10006. doi: 10.1029/2011GC003732
- Walker, A. M., & Wookey, J. (2012). MSAT—A new toolkit for the analysis of elastic and seismic anisotropy. *Computers & Geosciences*, 49, 81–90. doi: 10.1016/j.cageo.2012.05.031
- Walpole, J., Wookey, J., Kendall, J.-M., & Masters, T.-G. (2017). Seismic anisotropy and mantle flow below subducting slabs. *Earth and Planetary Science Letters*,

465, 155–167.

- Walsh, E., Arnold, R., & Savage, M. K. (2013). Silver and Chan revisited. *Journal of Geophysical Research: Solid Earth*, 118(10), 5500–5515. doi: 10.1002/jgrb.50386
- Walte, N. P., Heidelbach, F., Miyajima, N., Frost, D. J., Rubie, D. C., & Dobson, D. P. (2009). Transformation textures in post-perovskite: Understanding mantle flow in the D'' layer of the Earth. *Geophysical Research Letters*, 36, L04302. doi: 10.1029/2008GL036840
- Wang, Y., Hilairer, N., Nishiyama, N., Yahata, N., Tsuchiya, T., Morard, G., & Fiquet, G. (2013). High-pressure, high-temperature deformation of CaGeO_3 (perovskite) $\pm\text{MgO}$ aggregates: Implications for multiphase rheology of the lower mantle. *Geochemistry, Geophysics, Geosystems*, 14(9), 3389–3408.
- Wang, Y., & Wen, L. (2007). Complex seismic anisotropy at the border of a very low velocity province at the base of the Earth's mantle. *Journal Of Geophysical Research-Solid Earth*, 112(B9), B09305. doi: 10.1029/2006JB004719
- Wenk, H.-R., Cottaar, S., Tomé, C. N., McNamara, A. K., & Romanowicz, B. (2011). Deformation in the lowermost mantle: From polycrystal plasticity to seismic anisotropy. *Earth and Planetary Science Letters*, 306(1-2), 33–45. doi: 10.1016/j.epsl.2011.03.021
- Wenk, H.-R., Lonardeli, I., Pehl, J., Devine, J., Prakapenka, V., Shen, G., & Mao, H.-K. (2004). In situ observation of texture development in olivine, ringwoodite, magnesiowüstite and silicate perovskite at high pressure. *Earth and Planetary Science Letters*, 226(3), 507–519. doi: 10.1016/j.epsl.2004.07.033
- Wentzcovitch, R. M., Tsuchiya, T., & Tsuchiya, J. (2006). MgSiO_3 postperovskite at D'' conditions. *Proceedings Of The National Academy Of Sciences Of The United States Of America*, 103(3), 543–546. doi: 10.1073/pnas.0506879103
- Wheeler, J. (2009). The preservation of seismic anisotropy in the Earth's mantle during diffusion creep. *Geophysical Journal International*, 178(3), 1723–1732. doi: 10.1111/j.1365-246X.2009.04241.x
- Wheeler, J. (2010). Anisotropic rheology during grain boundary diffusion creep and its relation to grain rotation, grain boundary sliding and superplasticity. *Philosophical Magazine*, 90(21), 2841–2864. doi: 10.1080/14786431003636097
- Wolf, J., Creasy, N., Pisconti, A., Long, M. D., & Thomas, C. (2019). An investigation of seismic anisotropy in the lowermost mantle beneath iceland. *Geophysical Journal International*. doi: 10.1093/gji/ggz312
- Wookey, J., & Dobson, D. P. (2008). Between a rock and a hot place: The core-mantle boundary. *Philosophical Transactions of the Royal Society of London Series A-Mathematical Physical and Engineering Sciences*, 366(1885), 4543–4557. doi: 10.1098/rsta.2008.0184
- Wookey, J., & Kendall, J.-M. (2007). Seismic anisotropy of post-perovskite and the lowermost mantle. In K. Hirose, J. Brodholt, T. Lay, & D. A. Yuen (Eds.), *Post-perovskite: The last mantle phase transition* (pp. 171–189). Washington, D.C., USA: American Geophysical Union Geophysical Monograph 174.
- Wookey, J., & Kendall, J.-M. (2008). Constraints on lowermost mantle mineralogy and fabric beneath Siberia from seismic anisotropy. *Earth and Planetary Science Letters*, 275(1-2), 32–42. doi: 10.1016/j.epsl.2008.07.049
- Wookey, J., Kendall, J.-M., & Rümpker, G. (2005). Lowermost mantle anisotropy beneath the north Pacific from differential S–ScS splitting. *Geophysical Journal International*, 161(3), 829–838. doi: 10.1111/j.1365-246X.2005.02623.x
- Wu, X., Lin, J.-F., Kaercher, P., Mao, Z., Liu, J., Wenk, H.-R., & Prakapenka, V. B. (2017). Seismic anisotropy of the D'' layer induced by (001) deformation of post-perovskite. *Nature Communications*, 8, 14669.
- Wu, Z., Justo, J. F., & Wentzcovitch, R. M. (2013). Elastic anomalies in a spin-crossover system: Ferroperriclite at lower mantle conditions. *Physical review let-*

- ters, 110(22), 228501.
- Wuestefeld, A., Al-Harrasi, O., Verdon, J. P., Wookey, J., & Kendall, J.-M. (2010). A strategy for automated analysis of passive microseismic data to image seismic anisotropy and fracture characteristics. *Geophysical Prospecting*, 58(5), 753-771. doi: 10.1111/j.1365-2478.2010.00891.x
- Yamazaki, D., & Karato, S. (2007). Lattice-preferred orientation of lower mantle materials and seismic anisotropy in the D'' layer. In *Post-perovskite: The last mantle phase transition* (pp. 69-78). Washington, D.C., USA: American Geophysical Union.
- Yamazaki, D., & Karato, S.-i. (2002). Fabric development in (Mg,Fe)O during large strain, shear deformation: implications for seismic anisotropy in Earth's lower mantle. *Physics of The Earth and Planetary Interiors*, 131(3-4), 251-267. doi: 10.1016/S0031-9201(02)00037-7
- Yamazaki, D., Yoshino, T., Ohfuji, H., Ando, J.-i., & Yoneda, A. (2006). Origin of seismic anisotropy in the D'' layer inferred from shear deformation experiments on post-perovskite phase. *Earth and Planetary Science Letters*, 252(3-4), 372-378. doi: 10.1016/j.epsl.2006.10.004
- Yang, R., & Wu, Z. (2014). Elastic properties of stishovite and the CaCl₂-type silica at the mantle temperature and pressure: An ab initio investigation. *Earth and Planetary Science Letters*, 404, 14-21. doi: 10.1016/j.epsl.2014.07.020
- Young, C. J., & Lay, T. (1990). Multiple phase analysis of the shear velocity structure in the D'' region beneath Alaska. *Journal of Geophysical Research: Solid Earth*, 95(B11), 17385-17402.
- Yu, S., & Garnero, E. J. (2018). Ultra-low velocity zone locations: A global assessment. *Geochemistry, Geophysics, Geosystems*, 19(2), 396-414.
- Zhang, S., Cottaar, S., Liu, T., Stackhouse, S., & Militzer, B. (2016). High-pressure, temperature elasticity of Fe-and Al-bearing MgSiO₃: Implications for the Earth's lower mantle. *Earth and Planetary Science Letters*, 434, 264-273.
- Zhong, S., Zuber, M. T., Moresi, L., & Gurnis, M. (2000). Role of temperature-dependent viscosity and surface plates in spherical shell models of mantle convection. *Journal of Geophysical Research: Solid Earth*, 105(B5), 11063-11082.